The Astrophysical Journal, 978:86 (21pp), 2025 January 01 https://doi.org/10.3847/1538-4357/ad9245
© 2024. The Author(s). Published by the American Astronomical Society.
OPEN ACCESS

A Systematic Search for Candidate Supermassive Black Hole Binaries Using Periodic Mid-infrared Light Curves of Active Galactic Nuclei

Di Luo[1,2], Ning Jiang[1,3], and Xin Liu[4,5,6]
[1] CAS Key Laboratory for Research in Galaxies and Cosmology, Department of Astronomy, University of Science and Technology of China, Hefei, 230026, People's Republic of China; jnac@ustc.edu.cn
[2] School of Physical Sciences, University of Science and Technology of China, Hefei, 230026, People's Republic of China
[3] School of Astronomy and Space Sciences, University of Science and Technology of China, Hefei, 230026, People's Republic of China
[4] Department of Astronomy, University of Illinois at Urbana-Champaign, Urbana, IL 61801, USA
[5] National Center for Supercomputing Applications, University of Illinois at Urbana-Champaign, Urbana, IL 61801, USA
[6] Center for Artificial Intelligence Innovation, University of Illinois at Urbana-Champaign, 1205 West Clark Street, Urbana, IL 61801, USA
Received 2024 May 24; revised 2024 November 9; accepted 2024 November 11; published 2024 December 26

Abstract

Periodic variability in active galactic nuclei (AGNs) is a promising method for studying subparsec supermassive black hole binaries (SMBHBs), which are a challenging detection target. While extensive searches have been made in the optical, X-ray, and gamma-ray bands, systematic infrared (IR) studies remain limited. Using data from the Wide-field Infrared Survey Explorer (WISE), which provides unique decade-long mid-IR light curves with a six-month cadence, we have conducted the first systematic search for SMBHB candidates based on IR periodicity. Analyzing a parent sample of 48,932 objects selected from about half a million AGNs, we have identified 28 candidate periodic AGNs with periods ranging from 1268 to 2437 days (in the observer frame), by fitting their WISE light curves with sinusoidal functions. However, our mock simulation of the parent sample indicates that stochastic variability can actually produce a similar number of periodic sources, underscoring the difficulty in robustly identifying real periodic signals with WISE light curves, given their current sampling. Notably, we find no overlap between our sample and optical periodic sources, which can be explained by a distinct preference for certain periods due to selection bias. By combining archived data from different surveys, we have identified a candidate exhibiting periodic behavior in both the optical and IR bands, a phenomenon that warrants further validation through observational tests. Our results highlight the potential of IR time-domain surveys, including future missions such as the Nancy Grace Roman Space Telescope, for identifying periodic AGNs, but complementary tests are still needed to determine their physical origins, such as SMBHBs.

Unified Astronomy Thesaurus concepts: Supermassive black holes (1663); Quasars (1319); Time domain astronomy (2109); Active galactic nuclei (16); Infrared astronomy (786)

1. Introduction

Supermassive black holes (SMBHs) are intriguing celestial objects that reside at the centers of galaxies (J. Kormendy & L. C. Ho 2013). When galaxies merge, it is anticipated that the central BHs will form binary systems, known as SMBH binaries (SMBHBs; M. C. Begelman et al. 1980). These binary systems offer valuable insights into various astrophysical phenomena, including galaxy formation (M. Colpi & M. Dotti 2011), gravitational-wave (GW) emission (S. A. Hughes 2009), and the evolution of SMBHs (D. Merritt 2013). More massive binaries are pulsar-timing array sources (e.g., Z. Arzoumanian et al. 2018), while less massive binaries are targeted by space-based experiments such as LISA (A. Klein et al. 2016). They provide a laboratory to directly test strong-field general relativity (S. A. Hughes 2009; J. Centrella et al. 2010).

However, despite their theoretical significance, the direct electromagnetic detection of close SMBHBs below subparsec separation has proven to be a challenging endeavor (see recent reviews, such as those by A. De Rosa et al. 2019; D. J. D'Orazio & M. Charisi 2023), while numerous SMBH pairs at larger scales have been identified through the presence of dual active galactic nuclei (AGNs; e.g., S. Komossa et al. 2003; H. Zhou et al. 2004; X. Liu et al. 2010; M. Koss et al. 2011; X. Liu et al. 2011, 2013, 2018; Y.-C. Chen et al. 2022). When a binary has exhausted its interactions with stars but has not approached close enough to emit significant gravitational radiation, its orbit does not have an obvious mechanism for decay. This longstanding challenge presents a major uncertainty in estimating the abundance of SMBHB mergers as GW sources. In theory, the bottleneck may be overcome in gaseous environments (e.g., A. Gould & H.-W. Rix 2000; J. Cuadra et al. 2009; D. Chapon et al. 2013; L. del Valle et al. 2015), in triaxial or axisymmetric galaxies (e.g., F. M. Khan et al. 2016; L. Z. Kelley et al. 2017), and/or by interacting with a third BH in hierarchical mergers (e.g., O. Blaes et al. 2002; G. Kulkarni & A. Loeb 2012; M. Bonetti et al. 2018).

A recent and promising approach for identifying potential close SMBHB candidates has emerged in the thriving field of time-domain astronomy, which focuses on analyzing the periodic light curves of AGNs. The periodicity observed in these light curves can arise from changes in the accretion rate onto the BHs (M. J. Graham et al. 2015b) or from the relativistic Doppler boost resulting from the highly relativistic motion of gas in the mini accretion disk around the smaller BH in the binary system (D. J. D'Orazio et al. 2015). Extensive research has been conducted using optical light curves to search for SMBHBs, and the methods employed in these studies have

Original content from this work may be used under the terms of the Creative Commons Attribution 4.0 licence. Any further distribution of this work must maintain attribution to the author(s) and the title of the work, journal citation and DOI.

become well established (M. J. Graham et al. 2015a; M. Charisi et al. 2016; Z.-Y. Zheng et al. 2016; T. Liu et al. 2019; Y. C. Chen et al. 2020; W. T. Liao et al. 2021; Y.-J. Chen et al. 2024). However, many of the known candidates have been shown to be subject to false positives, due to stochastic quasar variability (e.g., S. Vaughan et al. 2016). Additionally, recent findings suggest that some AGNs may display periodic variations only at some specific epochs (e.g., N. Jiang et al. 2022; S. O'Neill et al. 2022), further enhancing the difficulties of periodic searches. Furthermore, previous surveys were only sensitive to the most massive quasars at high redshift ($z \gtrsim 2$) that should have already gone through their major-merger process (e.g., Y. Shen 2009). Regardless of the process that imprints periodicity, it is generally accepted that the timescale is primarily determined by the binary orbital period. SMBHBs with masses between 10^6 and $10^{10}\,M_\odot$ and separations of 0.01 pc possess orbital periods that span from years to several decades, making them possibly detectable by current time-domain surveys. In addition to the optical band, the periodic searches have also been conducted in other wavelength regimes, such as in the X-ray (T. Liu et al. 2020; R. Serafinelli et al. 2020) and gamma-ray bands (A. M. Holgado et al. 2018; A. Sandrinelli et al. 2018).

Periodic infrared (IR) light curves are also expected as a result of the reverberation mapping of the circumbinary dusty torus in periodic AGNs. However, the search for SMBHBs using IR data has not been extensively explored, despite the detection of an IR time lag in an individual SMBHB candidate (H. D. Jun et al. 2015), which highlights the potential of utilizing periodic IR light curves for SMBHB identification (D. J. D'Orazio & Z. Haiman 2017). The IR band not only provides an alternative approach to searching for SMBHBs, but also offers distinct advantages. First, IR photons are less susceptible to dust extinction, allowing them to penetrate through obscuring material, which is often abundant in galactic nuclear regions and galaxy merger systems. By extending the search to the IR wavelength range, we can uncover a population of SMBHB candidates that may have been previously overlooked, thereby expanding our knowledge of the prevalence and characteristics of these elusive systems. Even for unobscured AGNs, the variability amplitudes in the mid-IR band are typically larger compared to the optical band, due to lower background contamination. Additionally, as discussed in D. J. D'Orazio & Z. Haiman (2017), the dust-echo model can assist in determining the origin of central periodicity and place constraints on the physical characteristics of SMBHBs and their dust tori. To address this, we perform the first systematic search for SMBHB candidates via periodic IR light curves. The data we use come from the Wide-field Infrared Survey Explorer (WISE; E. L. Wright et al. 2010) and its successor NEOWISE (A. Mainzer et al. 2014), which have provided us with a public data set from 2010 February to 2023 December with a half-year cadence, except for a 2.5 yr gap for each object. In this study, we primarily focus on sinusoidal periodic signals, which have been commonly adopted in modeling the optical light curves of SMBHB candidates (e.g., D. J. D'Orazio et al. 2015) and on modeling the IR light curves using the dust-echo model (D. J. D'Orazio & Z. Haiman 2017).

The paper is structured as follows. Section 2 introduces the data and methods employed to search for periodic IR AGNs. Section 3 presents the search and corresponding analysis results, where we show compelling evidence demonstrating the highly improbable nature of these periodic light curves being generated by random processes. Section 4 compares selected candidates with normal AGNs and with previous studies that utilized optical light curves. Additionally, we discuss Sloan Digital Sky Survey (SDSS) J140336.43+174136.1 as a candidate exhibiting periodic behavior in both the optical and IR bands. Finally, we summarize the main results and suggest directions for future work in Section 5. We assume a cosmology with $H_0 = 66.88\,\mathrm{km\,s^{-1}\,Mpc^{-1}}$, $\Omega_m = 0.32$, and $\Omega_\Lambda = 0.68$, adopted from Planck Collaboration et al. (2020).

2. Data and Methods

2.1. IR Data

WISE was originally launched to conduct a full-sky survey in four mid-IR bands centered at 3.4, 4.6, 12, and 22 μm (labeled W1–W4) from 2010 February to August (E.L. Wright et al. 2010). The solid hydrogen cryogen used to cool the W3 and W4 instrumentation was depleted later and the spacecraft was placed in hibernation in 2011 February. However, it was reactivated in 2013 October under the new name NEOWISE-R, with only W1 and W2 operational, specifically to search for asteroids that could potentially pose a threat of impact on Earth (A. Mainzer et al. 2014). WISE and its new mission NEOWISE operate in the same manner—that is, scanning a specific sky area every six months, with an average of 12 or more individual exposures being taken within each epoch, typically spanning a single day. Consequently, each target in the sky has been observed 22–23 times, separated by a six month interval, up to 2023 December.

The single-exposure photometry of WISE and NEOWISE is archived in the AllWISE Multiepoch Photometry Table and the NEOWISE-R Single Exposure (L1b) Source Table,[7] respectively. The photometry we adopted is measured by point-spread function profile fitting, which is suitable for quasars. We first binned the data within each epoch, since the intraday IR variability is negligible except for very radio-loud AGNs (N. Jiang et al. 2012) and the anticipated periods we aim to detect are on much longer timescales. The variance of the binned data was recalculated as shown in Equation (1):

$$[\delta \mathrm{mag}(t_i)]^2 = \frac{1}{n_i - 1}\sum_{j=1}^{n_i}[\mathrm{mag}_j - \mathrm{mag}(t_i)]^2 + \frac{1}{n_i}\sigma_{s.s}^2, \quad (1)$$

where n_i denotes the number of data points within the ith epoch, $\mathrm{mag}(t_i)$ denotes the mean magnitude within the ith epoch, and σ_j denotes the photometric uncertainty of the jth data point. The first part represents the contribution from photometric uncertainty and short-term variability, while the second part represents the contribution from the system stability of WISE. We adopt $\sigma_{s.s.} = 0.029$ mag for WISE and $\sigma_{s.s.} = 0.016$ mag for NEOWISE, from J. Lyu et al. (2019).

Prior to binning, the data were filtered based on the quality flags in the catalog, following N. Jiang et al. (2021). Moreover, outliers that fell outside the 3σ range of the single data point at each epoch were eliminated, using the mean magnitude and mean photometric uncertainty at that epoch as references. The mean and variance of the single data points were then recomputed, resulting in the binned data used for our analysis.

[7] https://irsa.ipac.caltech.edu/cgi-bin/Gator/nph-scan?mission=irsa&submit=Select&projshort=WISE

This step was crucial to ensuring the accuracy and reliability of the data used in our study.

2.2. AGN Sample

The AGN sample we chose is the widely used Million Quasar Catalog (v8, 2023 August 2; E. W. Flesch 2023). This is a compendium of 907,144 type I QSOs and AGNs, largely complete from the literature up to 2023 June 30. 66,026 QSO candidates are also included, calculated via radio/X-ray association (including double radio lobes) as being 99% likely to be quasars. Blazars and type II objects are also included, bringing the total count to 1,021,800. To ensure the purity of our candidates, we only selected objects labeled as types "Q," "A," "B," "K," and "N" in the catalog, as these are confirmed AGNs. As a result, the number of objects amounts to 955,744. To enable a reliable long-term variability analysis, we apply a criterion that requires a minimum of 15 detected epochs (about two-thirds of all detected epochs) for each source. This left us with a subset of 576,260 AGNs.

In order to rationalize the computational effort in further analysis, we choose to analyze only AGNs with obvious variability. This selection strategy is crucial to ensuring that candidates meet the fifth selection criterion (see Section 2.4). Furthermore, light curves displaying subtle variability tend to pose a challenge in terms of model constraints within the damped random walk (DRW) framework (see Section 3.1). To address this issue, we introduce a requirement that, for a given light curve, at least one data point must satisfy $\mathrm{mag}(t_i) - 2\delta mag(t_i) > \mathrm{mag}_{\mathrm{mean}}$ and at least one data point should satisfy $\mathrm{mag}(t_i) + 2\delta\mathrm{mag}(t_i) < \mathrm{mag}_{\mathrm{mean}}$. This allows us to narrow down our sample to 53,496 AGNs, ensuring that the selected candidates have the necessary characteristics for further analysis. We also require that the light curves be well constrained by the DRW model (see Section 3.1), resulting in a parent sample of 48,932 AGNs.

2.3. Finding Periodicity

To identify sources exhibiting periodic variability, we employed a sinusoidal function to fit the light curves of both the W1 and W2 bands. The fitting process involved minimizing the following equation using the χ^2 statistics, as Equation (2) below (D. J. D'Orazio & Z. Haiman 2017):

$$\chi^2 = \sum_{i=1}^{n} \frac{[\mathrm{mag}(t_i) - A\sin\Omega(t_i - t_0) + B]^2}{[\delta\mathrm{mag}(t_i)]^2}. \quad (2)$$

The Lomb–Scargle (LS) periodogram (N. R. Lomb 1976; J. D. Scargle 1982) is widely used for periodicity detection in unevenly sampled data. In our analysis, we utilized the generalized LS (GLS) periodogram (M. Zechmeister & M. Kürster 2009) implemented in the `pyastronomy`[8] package. In the GLS periodogram, we calculate a series of "powers," defined as Equation (3):

$$p = \frac{\chi_0^2 - \chi^2}{\chi_0^2}, \quad (3)$$

where χ_0^2 is the residual of a model assuming no variability and χ^2 is equivalent to Equation (2) in the GLS periodogram (M. Zechmeister & M. Kürster 2009). Compared to the LS periodogram, the GLS periodogram provides a more accurate frequency prediction, by taking into consideration an offset and weights, which allows the calculation of the maximum power in the GLS periodogram to be equivalent to minimizing Equation (2). The searched period range of the GLS periodogram is from 700 to T_0 days, where T_0 is the time span of the light curve.

2.4. Selection Criteria

We selected reliable periodic candidates based on five criteria. First, to account for stochastic red-noise variability, we adopt a comparative approach, by measuring the performance of the candidates against that of simulated light curves, as described in Section 3.1. Rather than applying a single threshold to the normalized periodograms, we require 3σ significance in both the W1 and W2 bands.

Second, we adopt the signal-to-noise ratio defined as Equation (4) (J. H. Horne & S. L. Baliunas 1986), where A_0 denotes the amplitude and σ_r^2 denotes the variance of the residuals. We require that $\xi > 2$ for both the W1 and W2 bands:

$$\xi = A_0^2/(2\sigma_r^2). \quad (4)$$

Third, we require that the difference between the frequencies of the W1 and W2 light curves must not exceed 5% of their sum, in accordance with Equation (5):

$$\frac{|f_1 - f_2|}{f_1 + f_2} < 0.05, \quad (5)$$

where f_1 and f_2 represent the frequencies of the W1 and W2 light curves. In addition, the phase difference between them must be less than one-eighth of a cycle. This criterion reflects the requirements of the dust-echo model and guarantees that the two sinusoids have the same frequency and phase. However, we allow for a margin of error of one-eighth of a cycle to account for potential minor phase differences arising from low photometric accuracy or the intrinsic characteristics of the IR light curves. For instance, the W2 band may receive a greater contribution from dust with lower temperatures located farther from the BH, leading to a slight delay in the W2 variability compared to the W1 band (J. Lyu et al. 2019). If the sources are located at high redshifts, i.e., $z > 2$, the W1 and W2 emission could mainly come from a relatively inner and outer part of the accretion disk, so a time delay could also be expected. We confirm this small delay for our candidates in Section 3.2.

Fourth, the available data are required to show more than two cycles in both the W1 and W2 bands. It is important to note that even strictly sinusoidal variations are difficult to distinguish from a simple stochastic process when the number of cycles N_{cyc} is $\lesssim$5 (S. Vaughan et al. 2016). Any finite light curve generated by the corresponding variability process represents only a snapshot of that process. The periodogram derived from this light curve will show power distributed around the actual power spectral density (PSD) continuum with some scatter. This scatter can create the appearance of spikes in the periodogram (e.g., see Figures 1 and 12), leading the light curve to seemingly exhibit a sinusoidal-like pattern over two to three cycles, even if the underlying PSD process is purely continuous. Therefore, these patterns can only be reliably distinguished with much longer time series spanning many (e.g., >four to five) cycles of the putative period. However,

[8] https://pyastronomy.readthedocs.io/en/latest/index.html

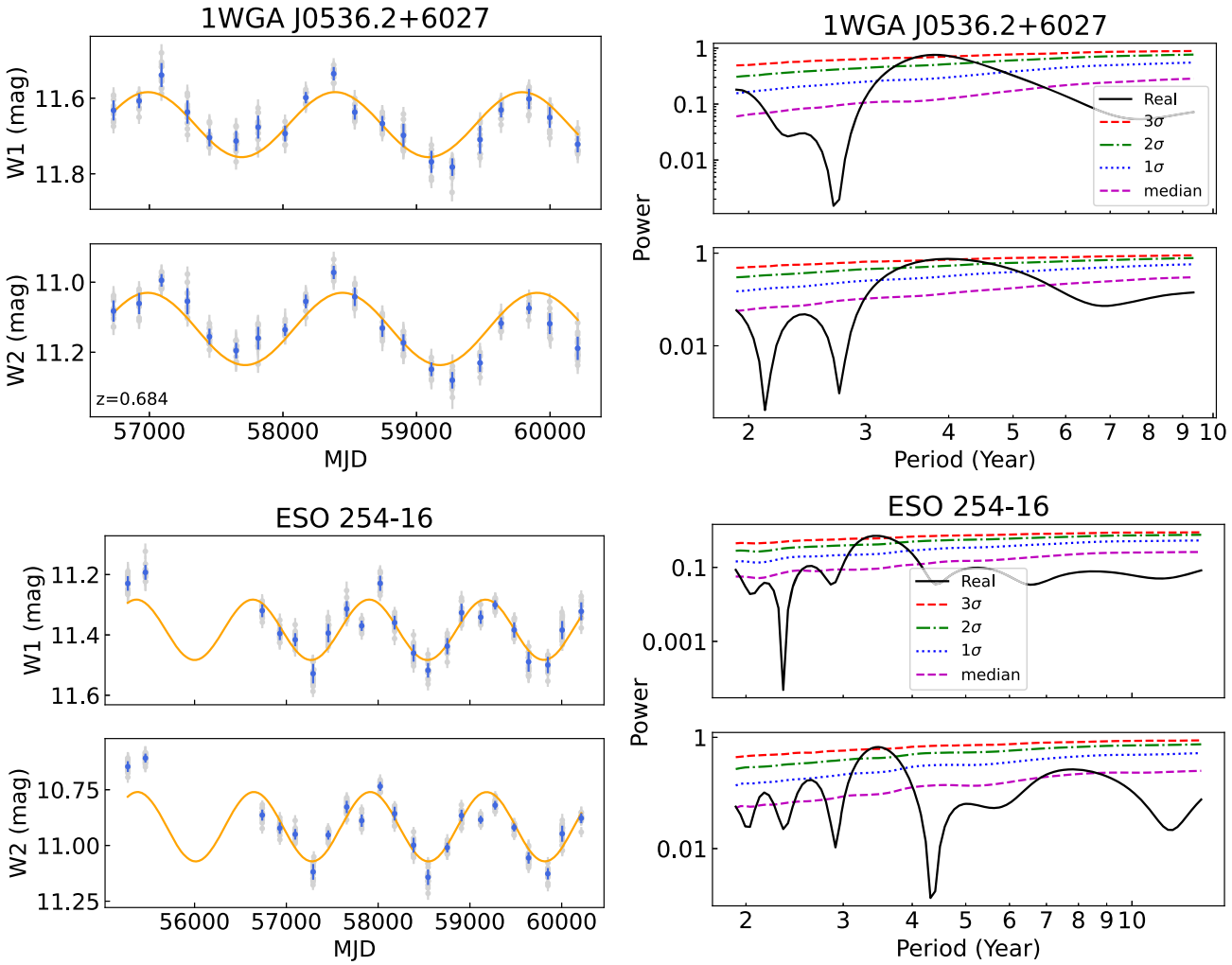

Figure 1. Two special examples of candidates. The top panel specifically highlights the highest-redshift source at $z = 0.684$ and the bottom panel highlights the candidate showing the most periods. Left: the gray error bars represent the original data (with outlier data points removed). The blue error bars represent the binned data. The orange sinusoids represent the best-fitting sine curves. Right: the black curves show the periodograms of candidates, while the other curves show different significance levels calculated from 100,000 simulated light curves.

most optical searches still adhere to a criterion of >1.5 cycles, due to the limited time span of the data (e.g., M. J. Graham et al. 2015a; M. Charisi et al. 2016; T. Liu et al. 2019; Y.-J. Chen et al. 2024). Consequently, false positives would arise in the candidate sample from stochastic red-noise variability (S. Vaughan et al. 2016). Due to the limited number of detected epochs, which amounts to 23, we set the limit to >two cycles. We believe that this is the best approach we can take with the current WISE data, but we note that further improvements should be pursued in future research with more available data.

Fifth, we check if the maximum power of the periodogram indicates a "correct" period, since anomalous data points (e.g., an outlier with a small error) could mislead the periodogram calculation. Additionally, this criterion allows us to check if the light curves show strong variability. We estimate the period of a light curve by examining the data points. If all data points within a time segment satisfy $\mathrm{mag}(t_i) - 2\delta\mathrm{mag}(t_i) > \mathrm{offset}$ (calculated by the periodogram), we classify it as a "faint segment." If all data points within a time segment satisfy $\mathrm{mag}(t_i) + 2\delta\mathrm{mag}(t_i) < \mathrm{offset}$, we classify it as a "bright segment." Then we conduct a count in chronological order, recording each change from a faint segment to a bright segment or vice versa and neglecting normal data points in this process (see the example shown in Figure 2). Denoting the total count as n, ideally $n/2$ periods would be included in the time span. We require that for both the W1 and W2 bands, the period at the maximum power $T_{\max}$ and the time span of the light curve T_0 satisfy Equation (6):

$$\frac{\max\{n-2,0\}}{2} < \frac{T_0}{T_{\max}} < \frac{n+3}{2}. \quad (6)$$

Figure 2 illustrates an AGN that meets all the selection criteria except for the fifth selection criterion in the W2 band. The periodogram analysis reveals a 3σ significance in the W2 light curve, indicating a period of $T_{\max} = 1545.6$ days within a time span of $T_0 = 4939.9$ days. However, the total count for W2 is 3, so it does not meet the fifth criterion. This failure is attributed to the lack of significant variability in the W2 band, as shown in Figure 2.

3. Analysis and Results

3.1. Simulating with Stochastic Variability

AGN variability can roughly be described by a Gaussian first-order continuous autoregressive model (B. C. Kelly et al. 2009),

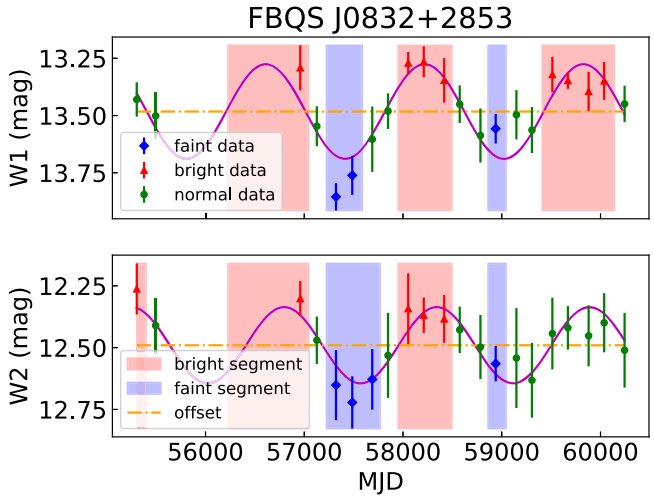

Figure 2. An example for the fifth selection criterion. In this example, the total count for W1 is 4, while W2 has 3 counts. Note that the error bars show 2δmag (t_i), and the purple lines show the best-fit sine curves.

also known as a DRW (C. L. MacLeod et al. 2010) or Ornstein–Uhlenbeck process. The likelihood function for the DRW process can be represented as

$$\mathcal{L} \propto |C|^{-\frac{1}{2}} \exp\left[-\frac{1}{2}\sum_{i,j}(X_i - q)(C^{-1})_{ij}(X_j - q)\right], \quad (7)$$

where the X_i represents the flux of the data point i and q is the long-term mean of the light curve. The covariance matrix C is given by

$$C_{ij} = \delta_{ij}\sigma_i^2 + \sigma^2 \exp\left(-\frac{|t_i - t_j|}{\tau}\right), \quad (8)$$

where δ_{ij} is the Kronecker delta. In our analysis, we assume a strong correlation between the W1 and W2 data. Subsequently, we have devised a modified form of the covariance matrix that accounts for this correlation, expressed as

$$C_{ai,bj} = \delta_{ab}\delta_{ij}\sigma_i^2 + [\rho + (1 - \rho)\delta_{ab}]\sigma^2 \exp\left(-\frac{|t_i - t_j|}{\tau}\right), \quad (9)$$

where a and b represent the observed band (W1 or W2) of the data points and ρ is the correlation coefficient.

Regarding the data quality of WISE, we only use the binned data when estimating DRW parameters. We set a uniform prior for the logarithm of the parameters σ_1, σ_2, and τ and a uniform prior for $\rho_{W1,W2}$. We set q as the mean magnitude of the light curve to reduce computational cost, and we use the Markov Chain Monte Carlo (MCMC) sampler `emcee`[9] (D. Foreman-Mackey et al. 2013) to construct the posterior samples of the parameters. However, we find that some light curves lack enough variability but pass the variability criterion (see Section 2.2) due to certain data points with very small errors. Consequently, they are not adequately constrained by the DRW model. To ensure a stable posterior for the MCMC processes, we set a criterion that the 1σ error of the posterior $lg\tau$ sample must be less than 2. This is the final requirement for defining our parent sample, resulting in a final number of 48,932 (see Section 2.2). The statistical distributions of σ, τ, and $\rho_{W1,W2}$ are illustrated in Figure 3. Upon comparison, the selected candidates exhibit similar values for σ_1, σ_2, and τ compared to the parent sample. Notably, they display a stronger correlation, which aids in meeting the fourth selection criterion more easily. The distribution of $\rho_{W1,W2}$ serves as validation for our correlation assumption.

As an alternative test, we perform a model selection to test if the correlation parameter is necessary to explain the light curve on top of an uncorrelated stochastic background. We adopt a maximum likelihood approach for the model comparison and parameter estimation. We use the Bayesian information criterion (BIC), which is defined as

$$\mathrm{BIC} = -2\ln\mathcal{L} + k\ln N, \quad (10)$$

where $\mathcal{L}$ is the likelihood function, k is the number of free model parameters, and N is the number of data points. A lower BIC value indicates a preferable model. Typically, when $\Delta\mathrm{BIC} < -10$, the model with the lower BIC is strongly favored. For the uncorrelated DRW process, we generate posterior parameter samples independently for each band. Subsequently, we integrate these samples into a covariance matrix to compute $\mathcal{L}$, with all correlation components set as zero. Our analysis indicates a strong preference for the correlated model over the uncorrelated one, aligning with our earlier analysis (further details are provided in Figure 4).

We proceed by randomly selecting a set of parameters to generate two correlated W1 and W2 simulated light curves. These simulated light curves are then compared with the actual observation cadence and measurement errors. This process is repeated 100,000 times to check that the selection criteria are met. In addition, we use the periodogram values of these simulated light curves to determine the significance of our candidates, as described in the first criterion in Section 2.4. To further validate our simulation methodology, we perform a statistical comparison between the real and simulated light curves. Our analysis shows that they exhibit similar behavior for each selection criterion (detailed results are given in Table 1), suggesting that the correlated DRW processes could potentially generate a comparable number of candidates to the real ones.

Notably, the DRW model is relatively simple and may not fully capture the complexity of actual AGN variability due to degeneracies (Y. Zu et al. 2013). When using the DRW assumption to calculate false-alarm probabilities (FAPs), it might not completely consider the assumptions of the red-noise hypothesis. However, using different variability models could lead to some small changes in the results, but usually not significant ones.

3.2. Candidates of Periodic Sources

Using the data and criteria outlined in Section 2, we have identified a total of 28 candidates. The catalog of candidates can be found in Table 2. The light curves and the GLS periodograms of two examples are presented in Figure 1 and the rest can be found in Figure 12. The W1 and redshift distributions of both the parent sample and the selected candidates are shown in Figure 5.

It is worth noting that the candidates are predominantly situated in the low-redshift range (median $z = 0.126$, with 27/28 at $z < 0.4$) and the bright region (median W1 = 12.69, 25/28

[9] https://emcee.readthedocs.io/en/stable/

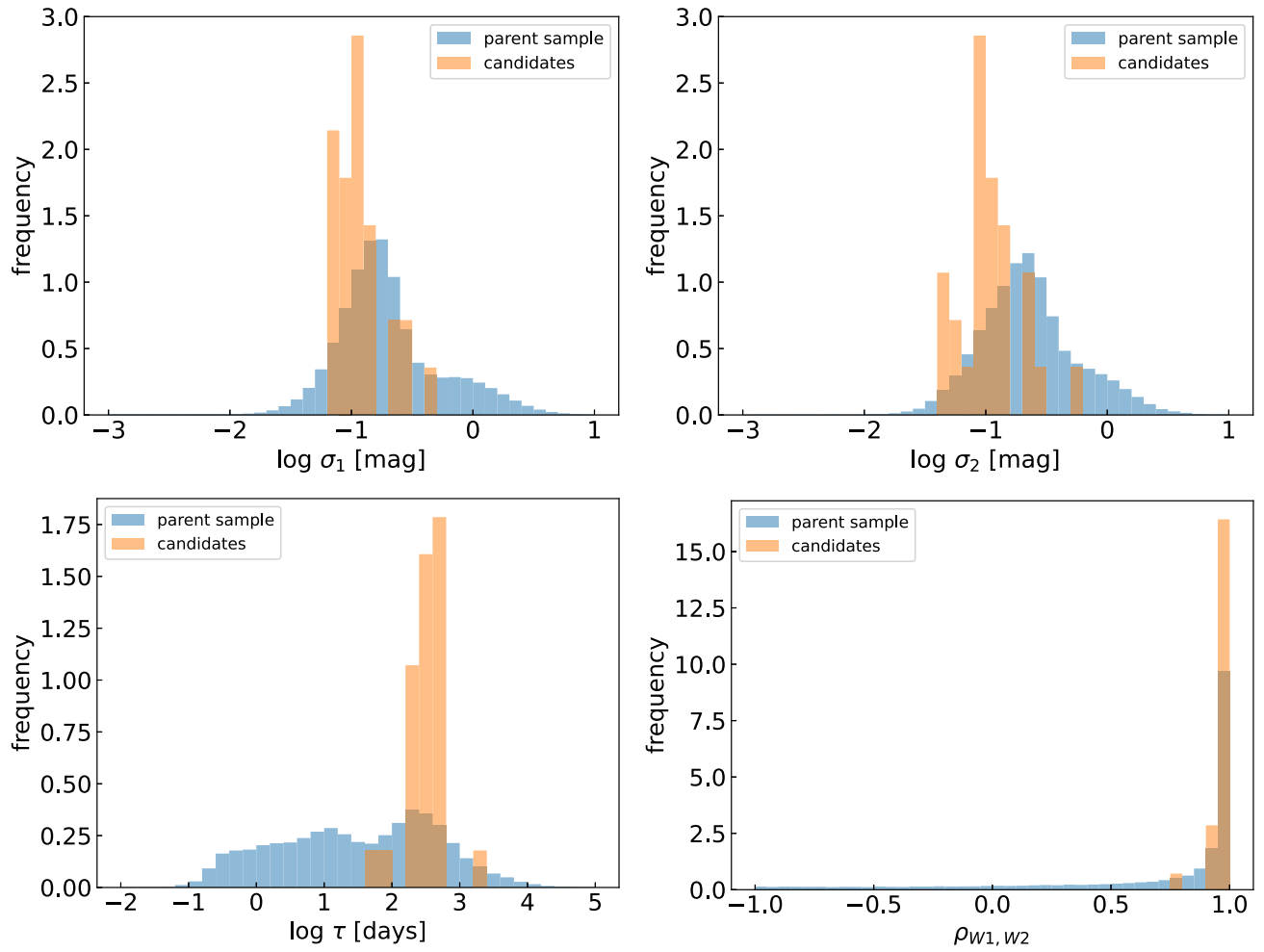

Figure 3. The DRW parameter distribution for the selection parent sample (blue) and the candidates (orange). Top: the σ distribution in the W1 band (left) and the W2 band (right). Bottom: the τ distribution (left) and the correlation coefficient distribution (right).

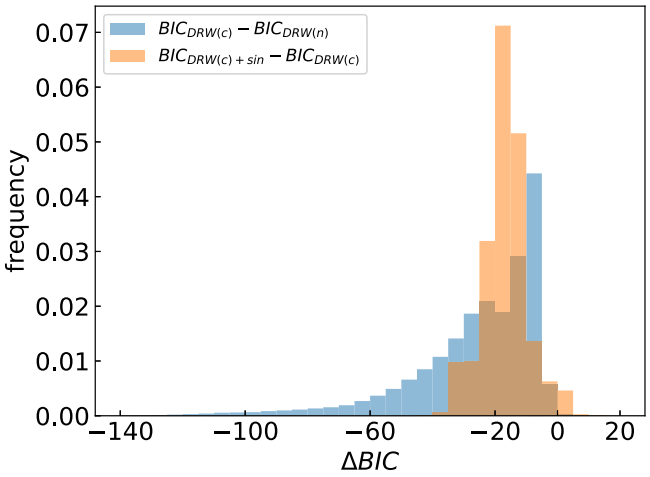

Figure 4. Distribution of the Δ BIC value. $BIC_{DRW(c)}$ is the BIC value of the correlated DRW model, $BIC_{DRW(n)}$ is the BIC value of the uncorrelated DRW model, while $BIC_{DRW(c)+sin}$ is the BIC value of the sinusoid +correlated DRW model for the candidates.

satisfying W1<14), which can be attributed to a selection effect making it easier for them to fulfill the selection criteria.

In Section 2.4, we mention the possibility of a slight phase delay between the W2 and W1 light curves. This is confirmed by our candidates, with an average delay of 0.025 periods, as illustrated in Figure 6. The maximum phase delay is 0.087 period, which remains smaller than the one-eighth of a period threshold used in our selection process, indicating a reasonable choice.

Table 1
Statistical Comparison between Real Light Curves and Simulated Ones

Constraints	Real	Mock
Number of AGNs	48,932	48,932
W1, 3σ significance	1075	1360
W2, 3σ significance	1099	1483
W1, $\xi > 2$	6360	8580
W2, $\xi > 2$	6724	9023
Close frequency and phase	19,590	21,194
W1, show >2 cycles	22,107	23,192
W2, show >2 cycles	21,987	23,561
W1, correct period	28,345	25,340
W2, correct period	27,886	25,145
Candidates	28	51.22

Note. The data in the "Mock" column refer to one-hundred-thousandth of the total of 4,893,200,000 simulated light curves, allowing direct comparison with the real data. "3σ significance" refers to the first selection criterion in Section 2.4, while "correct period" refers to the fifth selection in Section 2.4.

Table 2
The 28 Periodic AGN Candidates Meeting the Selection Criteria

Milliquas Name (1)	R.A. (2)	Decl. (3)	z (4)	W1 (5)	W2 (6)	Period (7)	Type (8)	log $L_{\rm bol}$ (9)	$\log(\frac{M_{\rm BH}}{M_\odot})$ (10)	log $\lambda_{\rm edd}$ (11)
PGC 3095405	4.3447	5.3532	0.11	11.582	10.585	1811	AX	⋯	⋯	⋯
PGC 1523911	10.1054	17.0707	0.112	12.216	11.578	1811	AR	⋯	⋯	⋯
ZOAG 139.33-5.77	41.0125	53.4745	0.035	11.909	11.016	2186	NX	⋯	⋯	⋯
1WGA J0536.2+6027	84.0463	60.4566	0.684	11.67	11.133	1428	QRX	⋯	⋯	⋯
ESO 254-16	91.6785	−43.7311	0.04	11.383	10.916	1268	NR	⋯	⋯	⋯
2MASS J06263670-4258059	96.6529	−42.9683	0.3	14.281	13.635	2019	BRX	⋯	⋯	⋯
RXS J07570+5832	119.2705	58.5445	0.168	12.658	11.709	1865	QX	⋯	⋯	⋯
SDSS J101241.21+215556.1	153.1717	21.9322	0.111	13.556	12.661	1863	A	44.46	7.79	−1.445
2MASX J11005099+5135026	165.2126	51.584	0.214	13.292	12.472	1829	ARX	45.19	8.69	−1.614
ESO 377-24	168.139	−36.4253	0.009	10.319	9.8026	1592	AR	⋯	⋯	⋯
ChaMP J115907.1+290842	179.7798	29.1452	0.227	13.594	12.66	2274	NRX	⋯	⋯	⋯
SDSS J124731.75+450121.3	191.8823	45.0226	0.214	12.822	11.937	2019	ARX	45.16	8.55	−1.498
SDSS J140336.43+174136.1	210.9018	17.6934	0.221	11.71	10.797	2346	QRX	45.81	9.63	−1.931
SDSS J143640.16+422933.8	219.1674	42.4927	0.216	13.939	13.061	2319	AR	44.9	8.46	−1.673
DESI 39632956414755490	219.6496	33.6835	0.216	13.43	12.487	2019	Q	⋯	⋯	⋯
SDSS J162938.09+362452.2	247.4087	36.4145	0.124	14.238	13.433	1829	AR	44.28	8.5	−2.338
SDSS J165822.32+183735.1	254.593	18.6264	0.177	12.782	11.957	2229	ARX	45.28	8.38	−1.213
IRAS 17020+4544	255.8766	45.6798	0.061	10.102	9.1251	1706	ARX	⋯	⋯	⋯
SDSS J171640.99+270544.1	259.1708	27.0956	0.228	14.168	13.223	2437	AX	44.34	6.8	−0.573
TXS 1919-166	290.6449	−16.5482	0.127	11.406	10.387	1941	AR2	⋯	⋯	⋯
6dF J193819.6-432646	294.5817	−43.4462	0.079	10.971	10.01	1903	AR	⋯	⋯	⋯
6dF J202557.4-482226	306.4891	−48.3739	0.067	11.059	10.197	2251	A	⋯	⋯	⋯
6dF J203052.8-345259	307.7199	−34.883	0.124	12.716	11.78	2186	AR	⋯	⋯	⋯
IGR J20450+7530	311.1435	75.533	0.095	12.797	12.084	2251	AX	⋯	⋯	⋯
SDSS J211655.57-013435.4	319.2316	−1.5765	0.206	13.472	12.557	1268	A	44.91	8.36	−1.562
6dF J214907.4-175159	327.2808	−17.8665	0.063	12.017	11.144	2039	AX	⋯	⋯	⋯
SDSS J215644.32-083529.3	329.1847	−8.5915	0.173	13.311	12.323	2297	A	44.83	7.92	−1.207
PGC 3096701	342.4148	11.008	0.083	11.519	10.668	1758	AX	⋯	⋯	⋯

Note. Columns (1)–(4): name, R.A., Decl., and redshift of the objects. Columns (5)–(6): median magnitudes in the W1 and W2 bands, respectively. Column (7): period (in the observer frame) in units of days. Column (8): Type/class from E. W. Flesch (2023): Q = QSO: type I, broad-line, core-dominated—860,100 of these; A = AGN: type I, Seyfert/host-dominated—47,044 of these; B = BL Lac–type object—2814 of these (FSRQs are typed as QSOs here); K = NLQSO: type II, narrowline, core-dominated—6048 of these; N = NLAGN: type II, Seyfert/host-dominated—39,768 of these; incomplete and includes an unquantified residue of legacy NELGs/ELGs/LINERs, plus some unclear AGNs—this is the catch-all category; and S = star, classified as a star but showing quasar-like photometry and radio/X-ray association, thus included as a quasar candidate—124 of these. Otherwise, R = radio association displayed; X = X-ray association displayed; and 2 = double radio lobes displayed (declared by data-driven algorithm). Columns (9)–(11): logarithmic bolometric luminosity, in units of erg per second; logarithmic BH mass, in units of solar mass; and logarithmic Eddington ratio for sources in the SDSS DR16Q catalog (Q. Wu & Y. Shen 2022) and the DR7 broad-line AGN catalog (H.-Y. Liu et al. 2019).

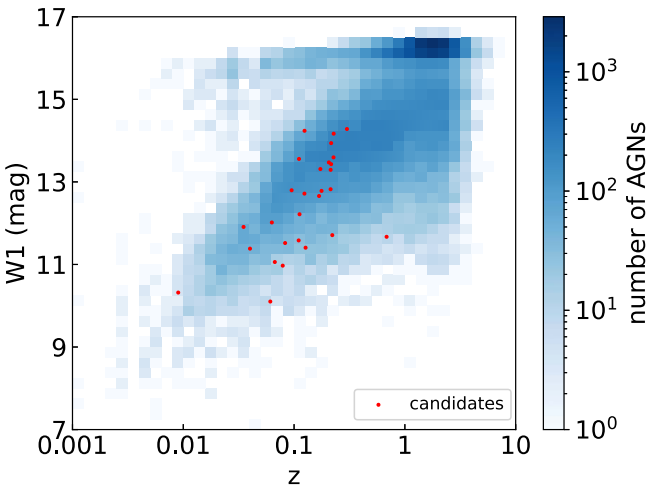

Figure 5. Distribution of the parent sample (blue) and the candidates (red) in the redshift and W1 magnitude space. We use a 40 × 40 grid to visualize the distribution of the parent sample. The color for each grid cell represents the number of AGNs from the parent sample that fall within that cell.

As an alternative test, here we use the BIC method (see the details in Section 3.1) to assess if an additional periodic signal is needed to explain the light curve on top of a stochastic background. The likelihood function for the DRW + sinusoidal model is written as

$$\mathcal{L} \propto |C|^{-\frac{1}{2}} \exp\left[-\frac{1}{2}\sum_{i,j}(X_i - S_i)(C^{-1})_{ij}(X_j - S_j)\right], \quad (11)$$

where S_i represents the sinusoid signal. Our analysis shows that for the vast majority of the candidates, $\mathrm{BIC_{DRW+sin}} - \mathrm{BIC_{DRW(c)}} < -10$, indicating robust evidence that the periodic model is significantly favored over the pure stochastic model (refer to Figure 4 for the detailed results). However, this could be explained by the limitation of the DRW model, which might not adequately capture a spiky PSD and may be more suited to smooth continuum-like PSD shapes. Therefore, additional data in the future are necessary to obtain a higher density in frequency sampling for the periodogram and to better test the preference for the sinusoid + DRW model.

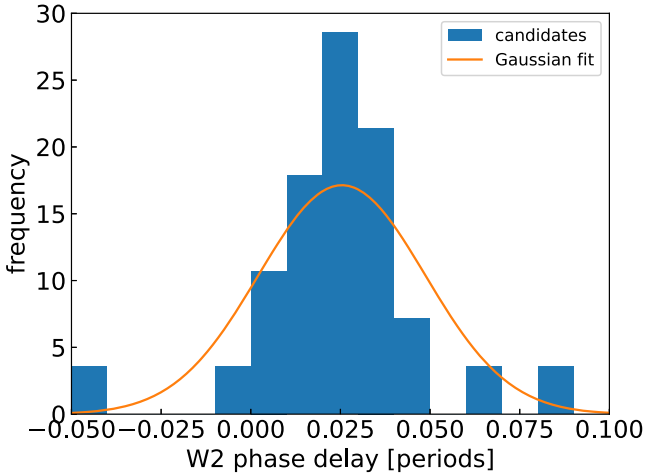

Figure 6. The distribution of the phase delay of W2 relative to W1 for the candidates (blue) and the corresponding Gaussian fit of the distribution (orange line).

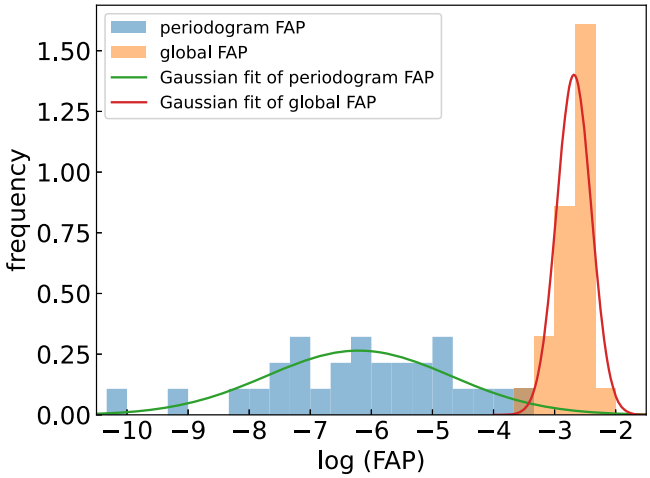

Figure 7. The FAP distribution estimated from periodogram calculation (blue) and the global FAP estimated from 100,000 simulated light curves (orange). The Gaussian fit curves for the two distributions are also shown.

It is worth noting that the sinusoid + DRW model is a commonly used model due to its simplicity and clear physical picture. However, there exist alternative light-curve models, such as the bursty model predicted by circumbinary accretion disk simulations (B. D. Farris et al. 2014). Despite the potential of this bursty model, we did not simulate it for our candidates, as we could not observe "bursty" characteristics in the WISE light curves.

Here, we compile the derived quantities for our analysis, which are presented in Table 2. The table includes essential information such as the Milliquas name, R.A., decl., redshift (z), and quasar properties, as provided by Q. Wu & Y. Shen (2022) and H.-Y. Liu et al. (2019). Additionally, we have included periodic properties such as the offsets of the W1 and W2 bands and the periods of the candidates.

3.3. FAP

To estimate the FAP for each candidate, we employ the method described in Y.C. Chen et al. (2020). We estimate the approximate FAP using the effective number of independent frequencies $N_{\rm eff}$, which is calculated by dividing the observed frequency window by the expected peak width $\delta f = 1/T$. The FAP is estimated as (e.g., J. T. VanderPlas 2018)

$$\mathrm{FAP} \sim 1 - [P_{\rm single}]^{N_{\rm eff}}, \tag{12}$$

where $P_{\rm single} = 1 - e^{Z}$, Z is the periodogram value defined in M. Zechmeister & M. Kürster (2009). Since candidates are selected based on the light curves of both the W1 band and W2 band, there are two $P_{\rm single}$ and $N_{\rm eff}$. To simplify the calculation, we can estimate the periodogram FAP as Equation (13):

$$\mathrm{FAP} \sim 1 - [P_{\rm single,W1}]^{N_{\rm eff,W1}} [P_{\rm single,W2}]^{N_{\rm eff,W2}}. \tag{13}$$

It is important to acknowledge that this calculation assumes independent FAPs for the W1 and W2 bands, contrary to the strong correlation observed in the DRW simulation (refer to Section 3.1). Nevertheless, this method provides an upper-limit estimate for the FAP, as single-band FAP calculations do not consider this correlation.

Additionally, we empirically compute the global FAP using the 100,000 simulated light curves for each AGN, following a similar approach as presented by A. J. Barth & D. Stern (2018).

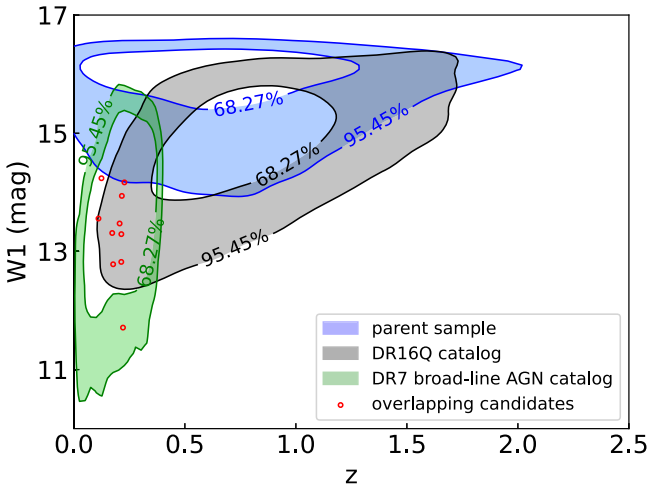

Figure 8. Distributions of the selection parent sample (blue), the quasars present in the DR16Q catalog that overlap with the parent sample (black), the AGNs present in the DR7 broad-line AGN catalog that overlap with the parent sample (green), and the overlapping candidates (red) in the redshift and W1 magnitude space. Enclosed percentiles are marked for each contour level.

Table 3
Statistical Comparison of Quasar Properties between Candidates and Control Samples

	Candidates	Control 1	Control 2
Mean of $\log(L_{\rm bol})$	44.92	44.70	44.84
SD of $\log(L_{\rm bol})$	0.45	0.29	0.37
Mean of $\log(M_{\rm BH})$	8.310	7.989	7.945
SD of $\log(M_{\rm BH})$	0.686	0.523	0.549
Mean of $\log(\lambda_{\rm edd})$	−1.505	−1.405	−1.216
Mean of $\log(f_d)$	−0.946	−0.813	−0.952
SD of $\log(f_d)$	0.160	0.224	0.399

Note. "Control 1" refers to the control sample that controls z and the W1 and W2 magnitudes. "Control 2" refers to the control sample that controls z and $L_{\rm bol}$.

The global FAP accounts for all false positives that satisfy all selection criteria within the explored frequency range. The global FAP values for candidates range from 4.0×10^{-4} to

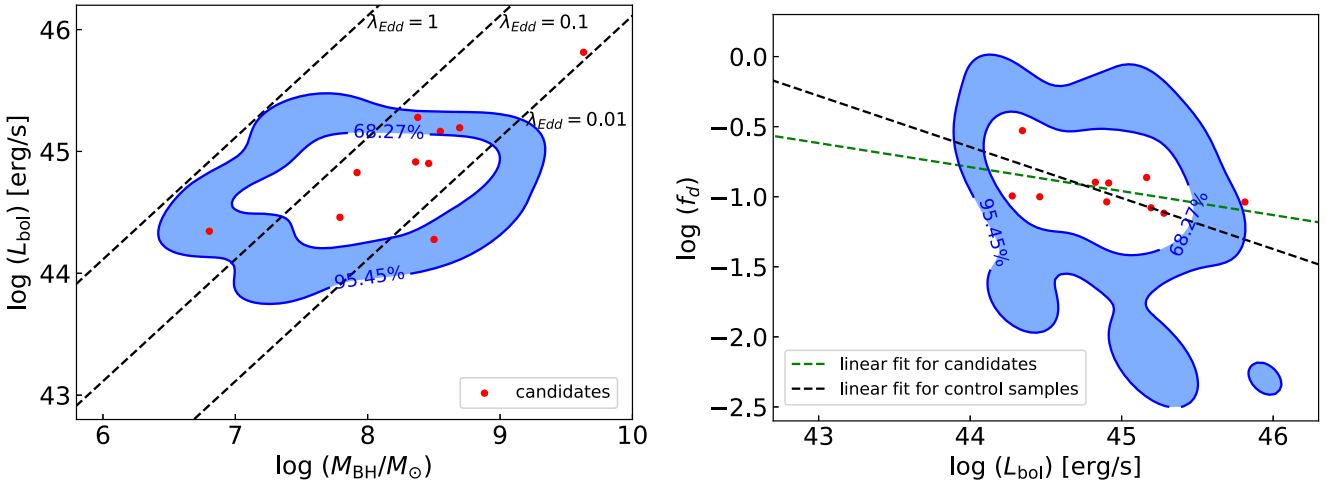

Figure 9. Left: distribution of the control samples (blue), which control for redshift, W1, and W2, and the candidates (red) in the log (M_{BH}) and log (L_{bol}) space. Right: distribution of the control samples (blue), which control for redshift and L_{bol}, and the candidates (red) in the log (L_{bol}) and log (f_d) space (right). The right panel also tests the anticorrelation between L_{bol} and f_d.

4.77×10^{-3}, with a mean of 2.07×10^{-3} by Gaussian fit. Further details are available in Figure 7.

It is noteworthy that the global FAPs are significantly higher than the periodogram FAPs. This discrepancy can be attributed to the stronger variability exhibited by the simulated light curves compared to real observations, leading to an increase in the global FAP. Moreover, while most false positives exhibit only a 3σ significance level, certain candidates display notably stronger significance, such as SDSS J162938.09+362452.2 and 6dF J214907.4-175159, as depicted in Figure 12.

4. Discussion

4.1. Do the Candidates Show Distinctive Properties?

One might wonder whether our selected periodic sample shows distinct features in other physical properties, such as bolometric luminosity (L_{bol}), BH mass (M_{BH}), and Eddington ratio ($\lambda_{edd} = L_{bol}/L_{edd}$). To investigate this, we try to extract a subsample of candidates with previous measurements in these parameters. We chose to crossmatch the candidates with two AGN samples based on SDSS, namely the SDSS DR16 quasar catalog (DR16Q; Q. Wu & Y. Shen 2022) and the DR7 broad-line AGN catalog (H.-Y. Liu et al. 2019). They contained 750,414 and 14,584 sources, concentrated at high and low redshifts, respectively (see Figure 8). We only found a total of 10 candidates that overlapped with the two catalogs.

Similar to the occupation of the candidates in the whole parent sample (see Figure 5), they are all in the low-redshift and low-magnitude space (see Figure 8), due to selection effects. Therefore, we need to construct a control sample for a fair comparison, at least in redshift and IR magnitudes. Specifically, we select the 10 closest AGNs with a redshift ratio less than 1.01 and with differences in W1 and W2 magnitudes less than 0.1. In cases where no AGN meets the specified criteria, we choose the closest AGN in the catalog as the control sample. After controlling, we then compare the M_{BH}, L_{bol}, and λ_{edd} of the periodic sources with normal AGNs. Additionally, we have also considered another parameter, the dust covering factor (f_d), defined as the ratio of the W1 monochromatic luminosity ($L_{W1} = \nu_{W1} F_{\nu W1}$) and the L_{bol} ($f_d = L_{W1}/L_{bol}$; e.g., X.-C. Ma & T.-G. Wang 2013), to indicate the extent of the dust obscuration. However, no significant differences in the distributions of these parameters can be seen visually (see Figure 9). We have also checked the means and standard deviations (SDs) of their distributions (see Table 3) and confirmed this.

We further performed the Kolmogorov–Smirnov (K-S) statistics for the L_{bol}, M_{BH}, λ_{edd}, and f_d distributions between the candidates and the control sample, yielding values of 0.375, 0.400, 0.225, and 0.400, respectively. The K-S tests suggest significant differences in these properties, with a critical value of 0.480 for a 95% confidence level, so none of them show significant differences. It is worth emphasizing that the systematic uncertainties in the estimates of AGN properties (e.g., a single-epoch BH mass; see the discussions in Y. Shen 2013) are non-negligible and would dilute the difference, if there were any. This may be particularly important for the small sample size for comparison here.

4.2. Comparison with SMBHB Candidates Selected by Optical Periodicity

As mentioned in the introduction, previous studies have identified samples of SMBHB candidates based on optical periodic light curves. It is intriguing to investigate whether there are any common sources between our IR-selected sample and these optically selected samples. Such overlap would provide compelling evidence for the periodicity of the candidates. Additionally, if the periods derived from optical light curves align with those obtained from IR light curves, we can employ the dust-echo model to further explore the properties of the candidates. For this purpose, we compile a collection of optical SMBHB candidates reported in various literature, including M. J. Graham et al. (2015a), M. Charisi et al. (2016), Z.-Y. Zheng et al. (2016), T. Liu et al. (2019), Y. C. Chen et al. (2020), and Y.-J. Chen et al. (2024).

Unfortunately, we do not find any overlap between our sample and those samples. The lack of matches is not entirely unexpected, as the two searches prioritize candidates with different periods. Specifically, we find that the periods of the optical candidates predominantly fell below 1700 days, whereas the periods of our selected candidates were mostly longer than 1700 days (see the details shown in Figure 10). Additionally, most of our candidates have low redshifts ($z < 0.4$), due to the

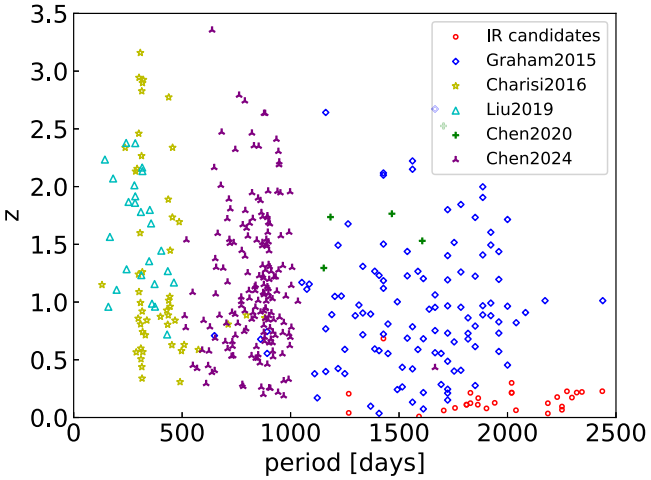

Figure 10. Redshift and period distributions of SMBHB candidates selected by this work (red) and those reported in previous works by optical search (other colors).

detection ability of WISE, while the redshifts of candidates from optical searches span from 0 to ∼3.

4.3. Optical Light Curves and a Possible Periodic Source

Given the abundance of optical photometric archival data, we then examined the optical light curves of the 28 candidates using data from various surveys, such as the Catalina Real-Time Transient Survey (A. J. Drake et al. 2009), the Palomar Transient Factory (A. Rau et al. 2009), the Zwicky Transient Facility (F. J. Masci et al. 2019), and the All-Sky Automated Survey for Supernovae (C. S. Kochanek et al. 2017). Their combined data set provides optical light curves spanning about two decades. We have normalized the data from different surveys and binned them at 20 days intervals. However, they generally show a small amplitude of optical variability, probably due to either intrinsically weak variability in the optical band or too shallow surveys. Only one candidate, SDSS J140336.43+174136.1, shows significant variability and periodicity in its optical light curve (see Figure 11).

The periodogram analysis of the optical light curve of SDSS J140336.43+174136.1 reveals a period of 2891 ± 22 days, which is slightly longer than the period fitted from the IR light curves, which is 2346 ± 87 days. The errors are given by periodogram peak statistics based on 100,000 perturbed light curves for each real light curve. The discrepancy could be caused by the poor cadence of the WISE surveys, and so in the following analysis we choose the optical period for this particular source.

We present the corresponding best-fitting sinusoids for the W1, W2, and optical light curves in Figure 11. The time delay between the W1 (W2) and optical light curves is 630 (727) days (in the rest frame), respectively. Assuming the simplest scenario of a hollow spherical shell of dust with the source located at its center, we can easily estimate that the inner radius of the shell is 0.53 pc. These values are roughly consistent with previous statistical correlations between the time delay and bolometric luminosity of AGNs. For example, using the relations obtained by J. Lyu et al. (2019), i.e.,

$$\Delta t_{\rm W1}/{\rm day} = 10^{2.10\pm0.06}(L_{\rm bol}/10^{11}L_{\odot})^{0.47\pm0.06} \quad (14)$$

for the W1 band and

$$\Delta t_{\rm W2}/{\rm day} = 10^{2.20\pm0.06}(L_{\rm bol}/10^{11}L_{\odot})^{0.45\pm0.05} \quad (15)$$

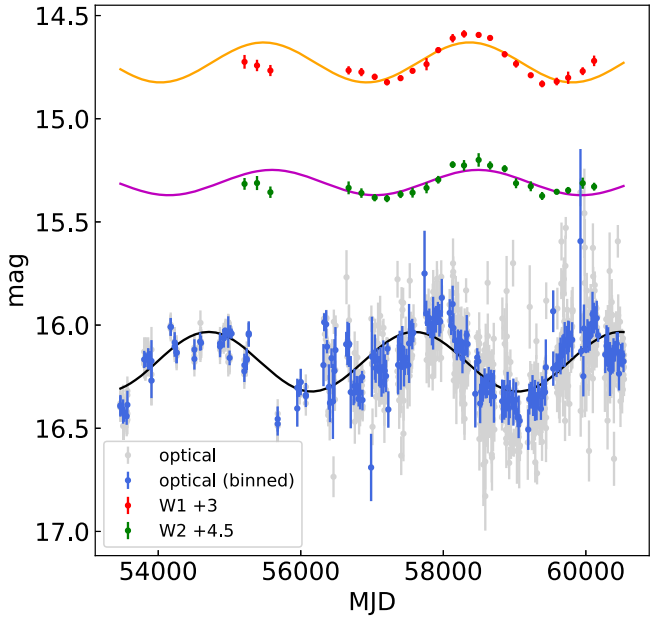

Figure 11. The W1, W2, and optical light curves of SDSS J140336.43 +174136.1. The orange, purple, and black lines represent the corresponding best-fitting sinusoids. We assume that the periods of the IR light curves are the same as those of the optical light curves.

for the W2 band, and a given bolometric luminosity of $10^{45.81}$ erg s^{-1} for SDSS J140336.43+174136.1 (see Table 2), the W1 and W2 time delays are estimated to be 476 ± 147 days and 566 ± 158 days, respectively, which is in good agreement with our measurements.

5. Conclusion

In this work, we have conducted the first systematic search for SMBHBs in the IR band and identified 28 AGNs exhibiting IR periodic variability using the decade-long WISE and NEOWISE light curves. We have performed extensive simulations to evaluate the potential influence of stochastic variability on candidate selection. By counting all the false positives in the simulated light curves, the probability of these periodic light curves being generated by random processes is an average of 0.207% by Gaussian fit. However, the number can be reproduced by our mock simulations with the DRW process of the parent sample. This indicates the challenge of identifying reliable SMBHBs with periodic emission using only WISE light curves, which are constrained by their time span and visit cadence, necessitating a low threshold on the minimum number of cycles ($N_{\rm cyc} > 2$). Consequently, the nature of these periodic sources, whether driven by SMBHBs or not, should be carefully tested in future observations. We subsequently investigated whether these IR periodic sources exhibit distinct properties compared to normal AGNs. However, no significant biases were found, and the small sample size prevents us from statistically identifying potential weak differences. On the other hand, we found that there is no overlap between our sample (IR-selected) and the SMBHB candidates reported in the literature (optically selected), likely due to differences in their preferred period ranges. Interestingly, we have identified SDSS J140336.43+174136.1 as a candidate displaying periodicity in both the optical and IR bands. Further extended and more sensitive observations of these candidates are essential to confirm whether or not they are

real periodic sources in both the optical and IR bands. As suggested by D. J. D'Orazio & Z. Haiman (2017), the periodic sources can also help test the physical mechanisms that produce the observed periodicity, due to relativistic Doppler modulation or accretion-rate fluctuations.

This study highlights the promising potential of identifying SMBHB candidates through IR time-domain observations, which can significantly complement searches in other bands, although there are challenges in distinguishing genuine sources. It opens up a new avenue for SMBHB searches and can be applied to future surveys. Although NEOWISE unfortunately ended on 2024 July 31, the upcoming NEO Surveyor (A. K. Mainzer et al. 2023), the successor to NEOWISE, and the Nancy Grace Roman Space Telescope (D. Spergel et al. 2015) will ensure a bright future for IR time-domain astronomy, particularly for SMBHB searches (Z. Haiman et al. 2023). These different surveys somewhat form a relay in time and provide us with IR light curves with a long time baseline, which is essential for verifying the periodicity of the candidates with $N_{\rm cyc} < 4$ and for detailed comparisons against physical models.

Acknowledgments

We sincerely thank the expert referee for very constructive and insightful comments, which helped improve our manuscript greatly. This work is supported by the Strategic Priority Research Program of the Chinese Academy of Sciences (grant No. XDB0550200), the National Natural Science Foundation of China (grants 12073025, 12192221), and science research grants from the China Manned Space Project and the Cyrus Chun Ying Tang Foundations. D.L. acknowledges the support from the National Undergraduate Training Program for Innovation and Entrepreneurship. X.L. acknowledges support by NSF grant AST-2206499. This research makes use of data products from WISE, which is a joint project of the University of California, Los Angeles, and the Jet Propulsion Laboratory/California Institute of Technology, funded by the National Aeronautics and Space Administration. This research also makes use of data products from NEOWISE-R, which is a project of the Jet Propulsion Laboratory/California Institute of Technology, funded by the Planetary Science Division of the National Aeronautics and Space Administration. This research has made use of the NASA/IPAC Infrared Science Archive, which is operated by the California Institute of Technology, under contract with the National Aeronautics and Space Administration.

Appendix
The IR Light Curves of the Periodic AGN Sample

We have shown the light curves of two special candidates in Figure 1. Here, we show the light curves of the other 26 candidates in Figure 12.

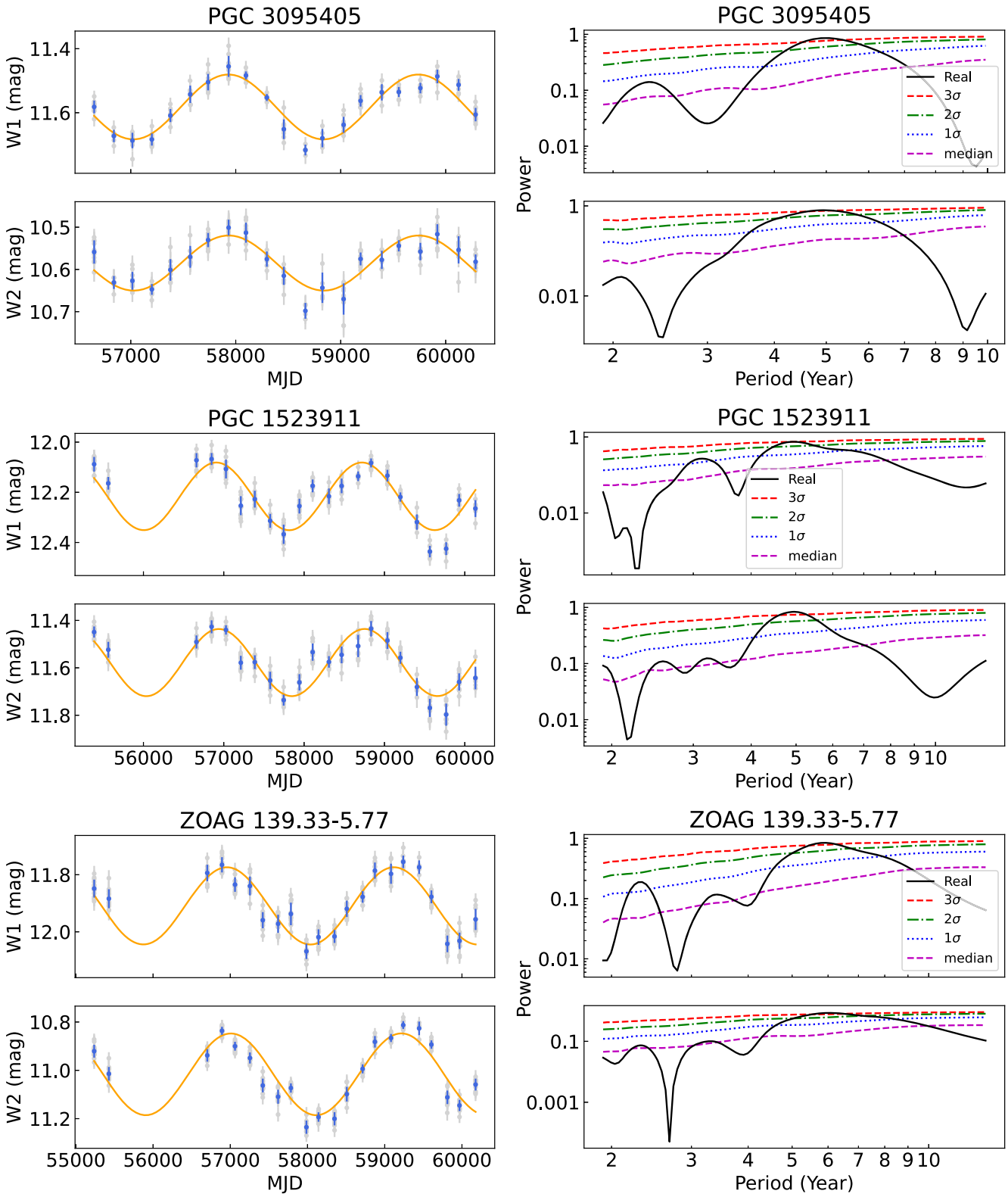

Figure 12. The light curves and periodograms of the other 26 candidates. The legends correspond to those in Figure 1.

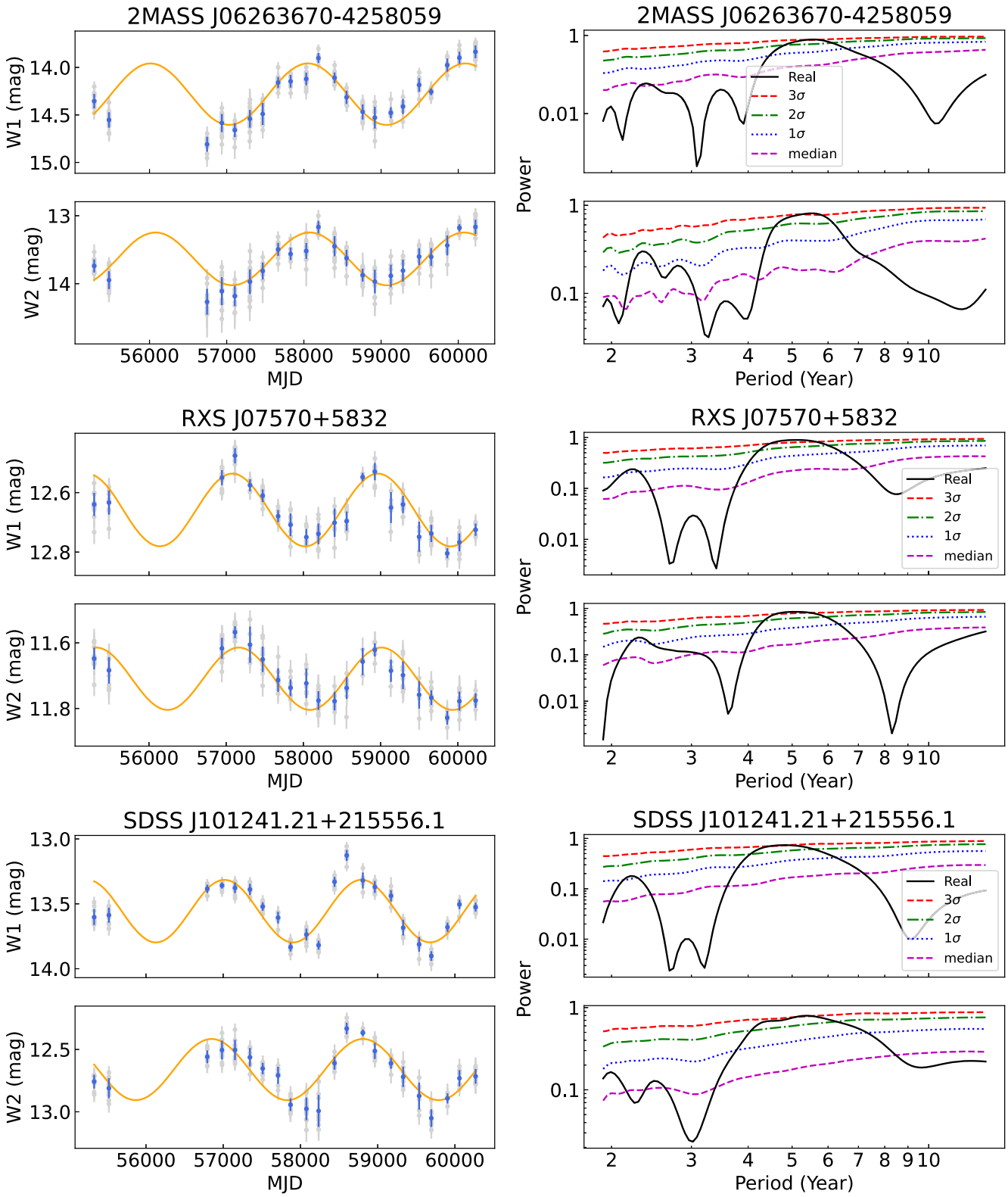

Figure 12. (Continued.)

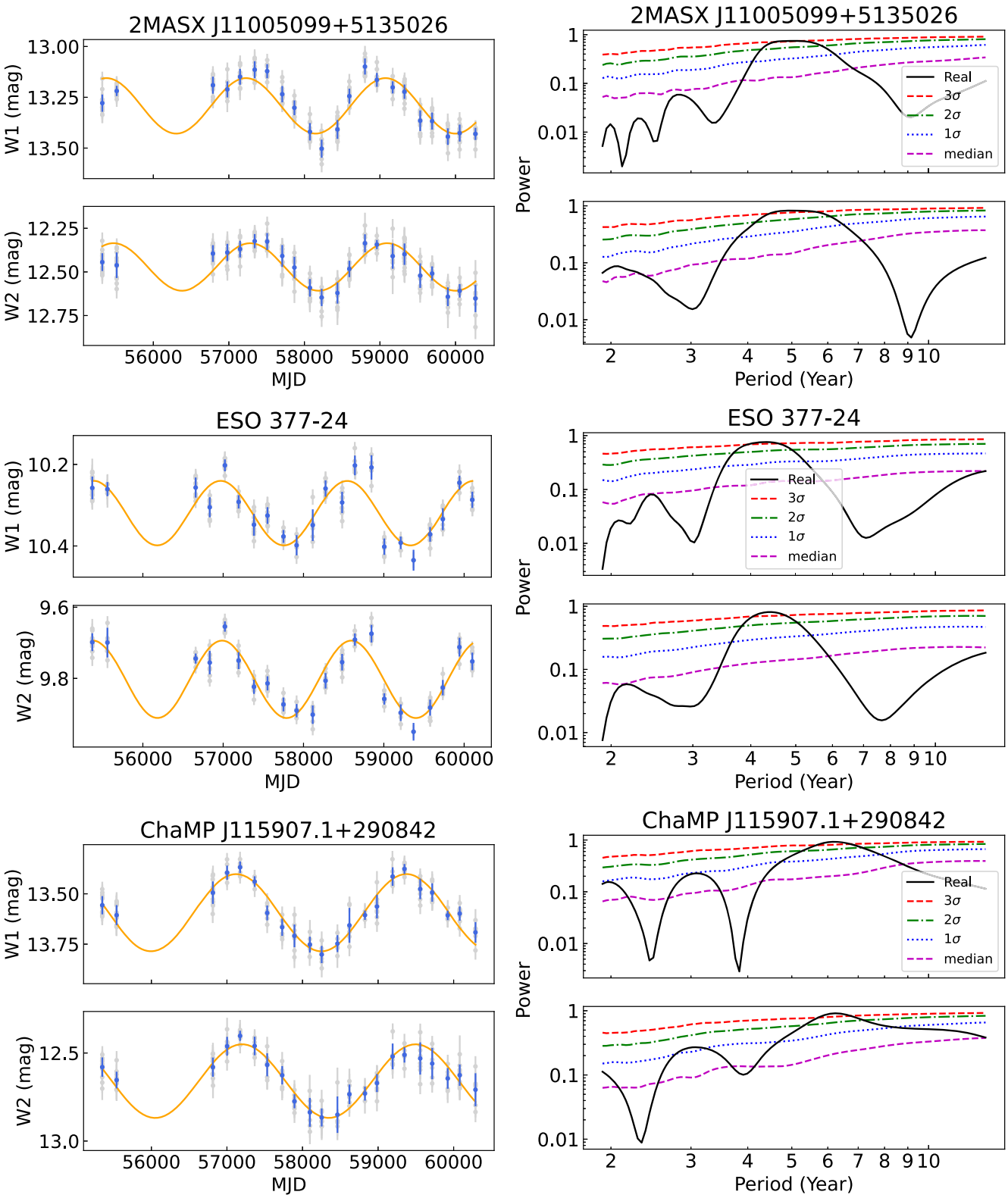

Figure 12. (Continued.)

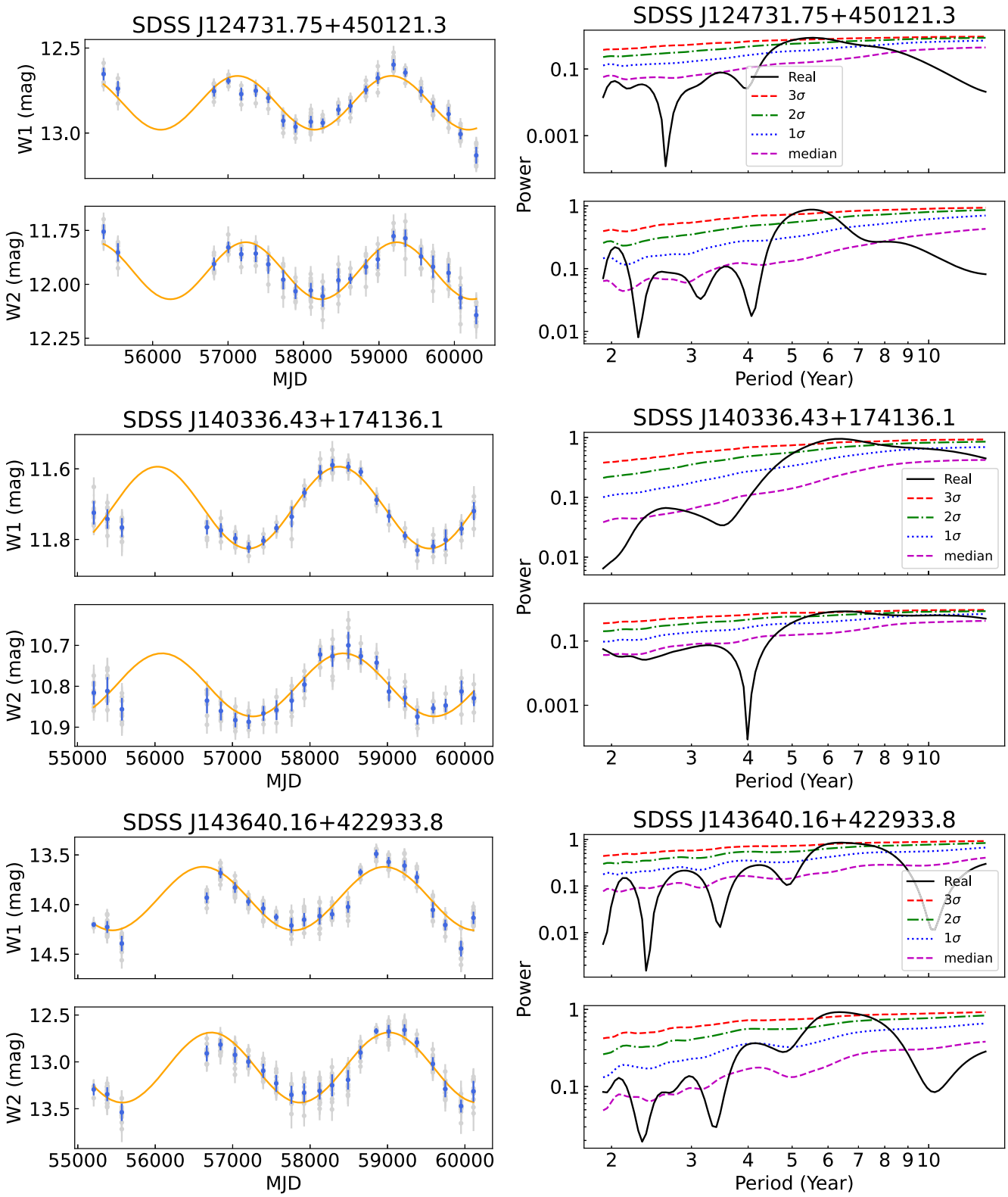

Figure 12. (Continued.)

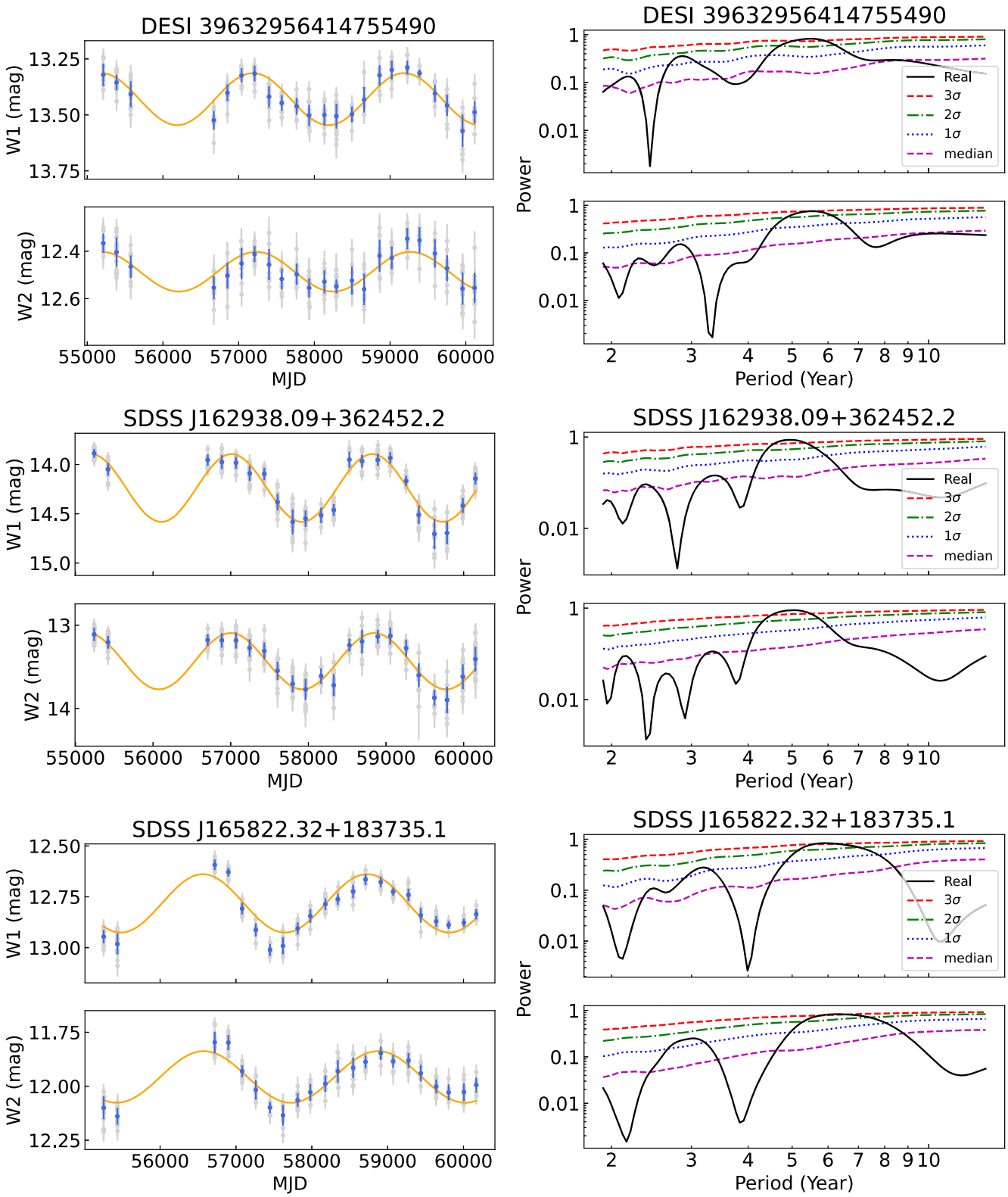

Figure 12. (Continued.)

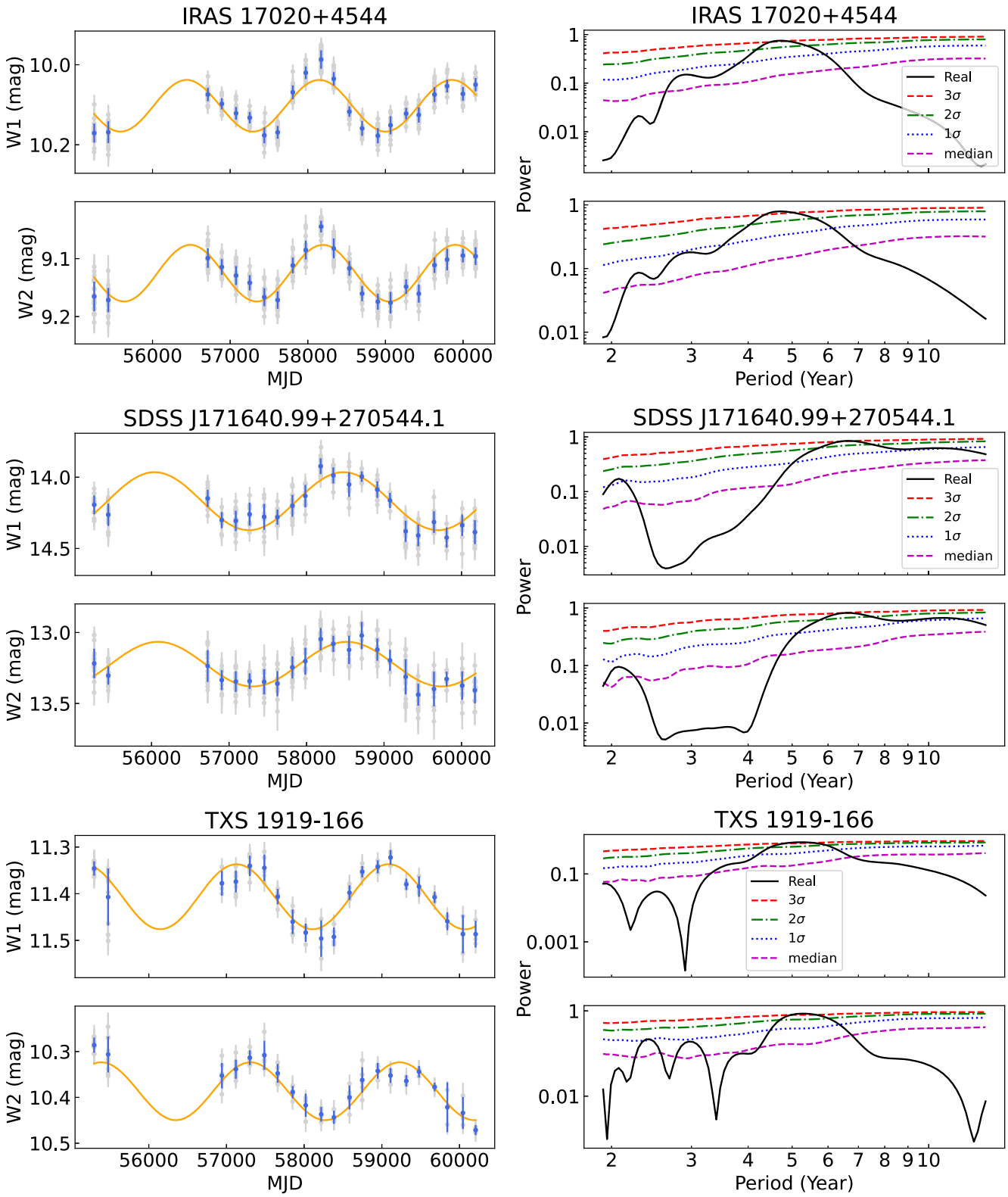

Figure 12. (Continued.)

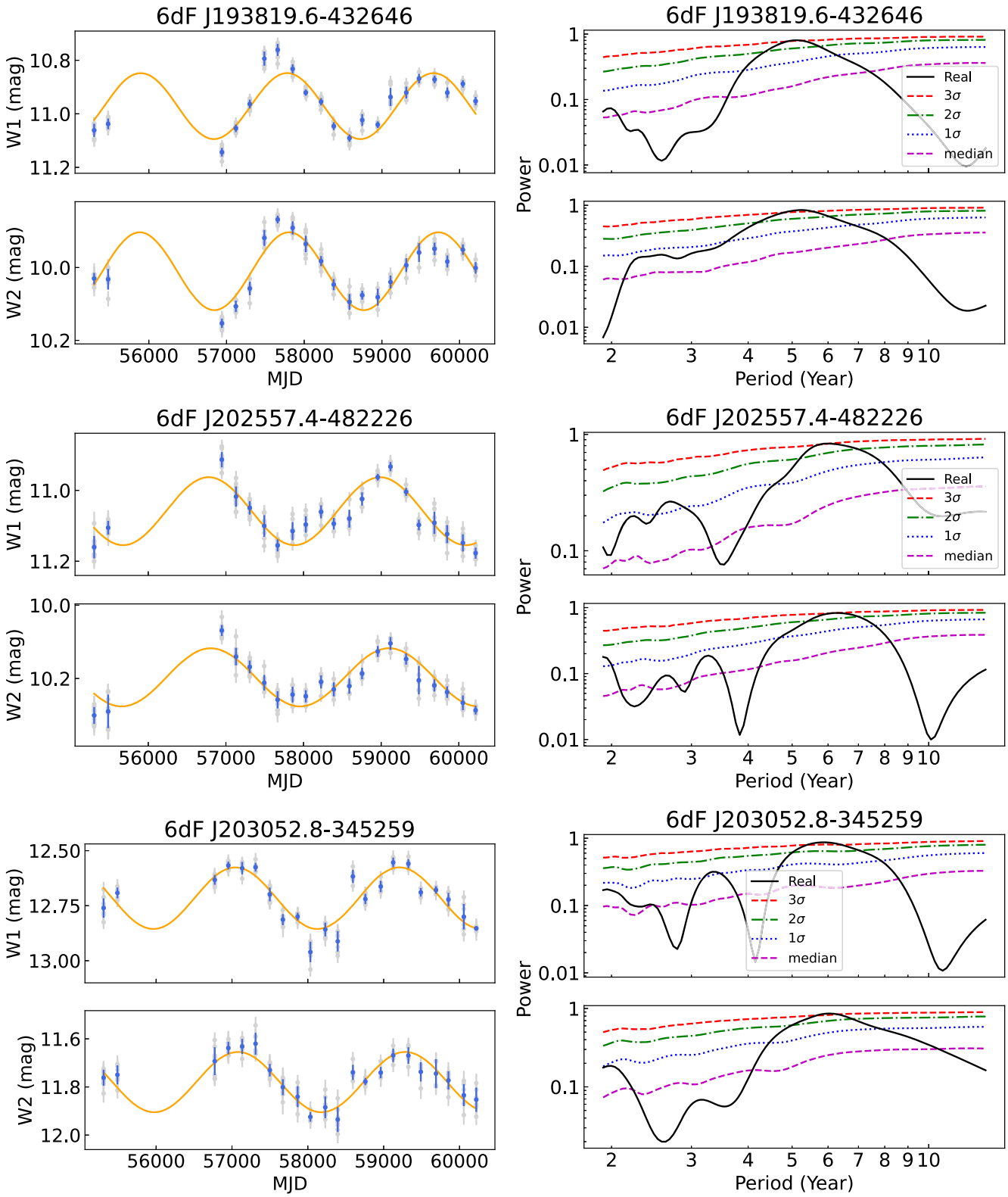

Figure 12. (Continued.)

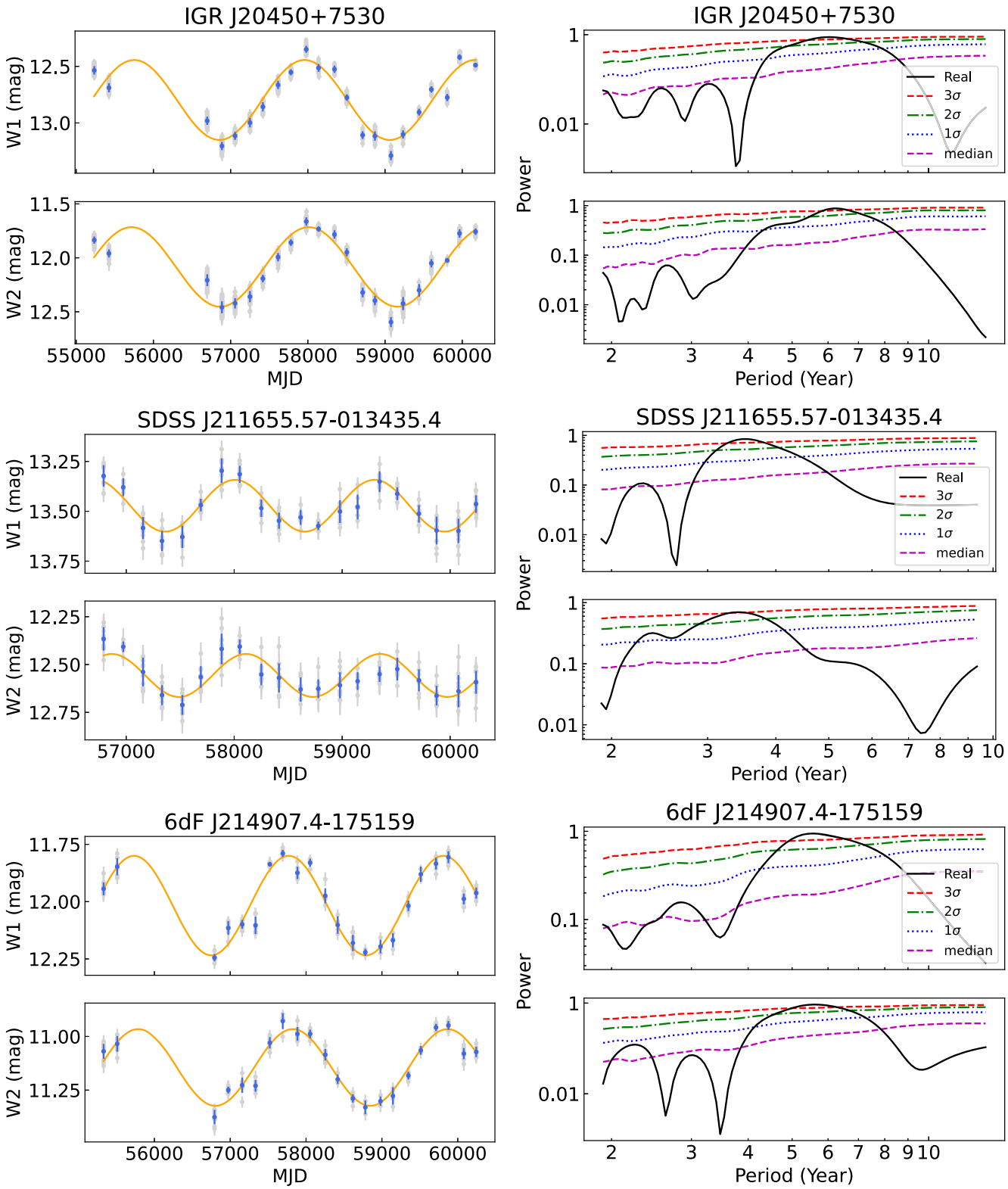

Figure 12. (Continued.)

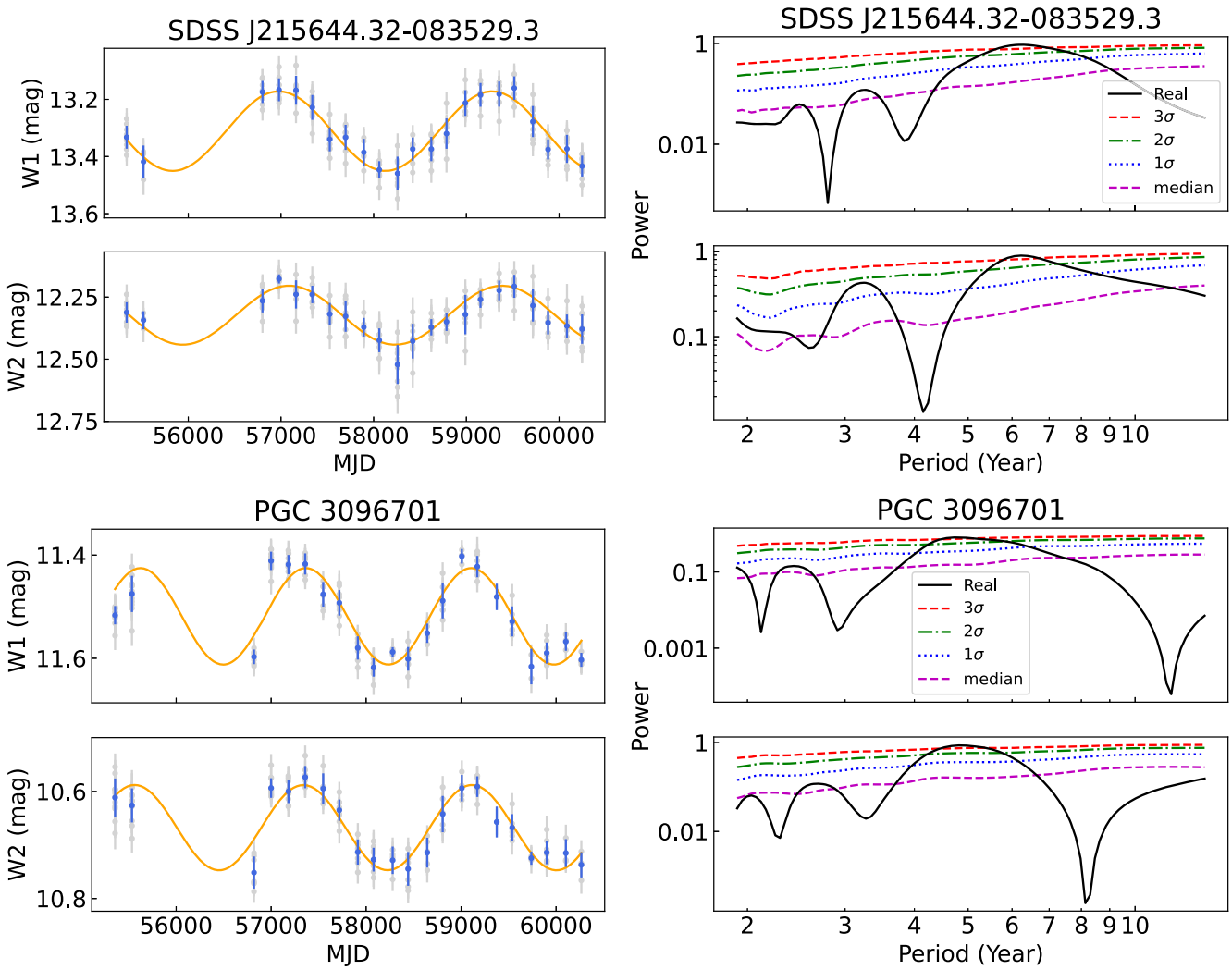

Figure 12. (Continued.)

ORCID iDs

Di Luo https://orcid.org/0009-0007-1153-8112
Ning Jiang https://orcid.org/0000-0002-7152-3621
Xin Liu https://orcid.org/0000-0003-0049-5210

References

Arzoumanian, Z., Baker, P. T., Brazier, A., et al. 2018, ApJ, 859, 47
Barth, A. J., & Stern, D. 2018, ApJ, 859, 10
Begelman, M. C., Blandford, R. D., & Rees, M. J. 1980, Natur, 287, 307
Blaes, O., Lee, M. H., & Socrates, A. 2002, ApJ, 578, 775
Bonetti, M., Sesana, A., Barausse, E., & Haardt, F. 2018, MNRAS, 477, 2599
Centrella, J., Baker, J. G., Kelly, B. J., & van Meter, J. R. 2010, RvMP, 82, 3069
Chapon, D., Mayer, L., & Teyssier, R. 2013, MNRAS, 429, 3114
Charisi, M., Bartos, I., Haiman, Z., et al. 2016, MNRAS, 463, 2145
Chen, Y.-C., Hwang, H.-C., Shen, Y., et al. 2022, ApJ, 925, 162
Chen, Y.-C., Liu, X., Liao, W.-T., et al. 2020, MNRAS, 499, 2245
Chen, Y.-J., Zhai, S., Liu, J.-R., et al. 2024, MNRAS, 527, 12154
Colpi, M., & Dotti, M. 2011, ASL, 4, 181
Cuadra, J., Armitage, P. J., Alexander, R. D., & Begelman, M. C. 2009, MNRAS, 393, 1423
De Rosa, A., Vignali, C., Bogdanović, T., et al. 2019, NewAR, 86, 101525
del Valle, L., Escala, A., Maureira-Fredes, C., et al. 2015, ApJ, 811, 59
D'Orazio, D. J., & Charisi, M. 2023, arXiv:2310.16896
D'Orazio, D. J., & Haiman, Z. 2017, MNRAS, 470, 1198
D'Orazio, D. J., Haiman, Z., & Schiminovich, D. 2015, Natur, 525, 351
Drake, A. J., Djorgovski, S. G., Mahabal, A., et al. 2009, ApJ, 696, 870
Farris, B. D., Duffell, P., MacFadyen, A. I., & Haiman, Z. 2014, ApJ, 783, 134
Flesch, E. W. 2023, OJAp, 6, 49
Foreman-Mackey, D., Hogg, D. W., Lang, D., & Goodman, J. 2013, PASP, 125, 306
Gould, A., & Rix, H.-W. 2000, ApJL, 532, L29
Graham, M. J., Djorgovski, S. G., Stern, D., et al. 2015a, MNRAS, 453, 1562
Graham, M. J., Djorgovski, S. G., Stern, D., et al. 2015b, Natur, 518, 74
Haiman, Z., Xin, C., Bogdanović, T., et al. 2023, arXiv:2306.14990
Holgado, A. M., Sesana, A., Sandrinelli, A., et al. 2018, MNRAS, 481, L74
Horne, J. H., & Baliunas, S. L. 1986, ApJ, 302, 757
Hughes, S. A. 2009, ARA&A, 47, 107
Jiang, N., Zhou, H.-Y., Ho, L. C., et al. 2012, ApJL, 759, L31
Jiang, N., Wang, T., Dou, L., et al. 2021, ApJS, 252, 32
Jiang, N., Yang, H., Wang, T., et al. 2022, arXiv:2201.11633
Jun, H. D., Stern, D., Graham, M. J., et al. 2015, ApJL, 814, L12
Kelley, L. Z., Blecha, L., & Hernquist, L. 2017, MNRAS, 464, 3131
Kelly, B. C., Bechtold, J., & Siemiginowska, A. 2009, ApJ, 698, 895
Khan, F. M., Fiacconi, D., Mayer, L., Berczik, P., & Just, A. 2016, ApJ, 828, 73
Klein, A., Barausse, E., Sesana, A., et al. 2016, PhRvD, 93, 024003
Kochanek, C. S., Shappee, B. J., Stanek, K. Z., et al. 2017, PASP, 129, 104502
Komossa, S., Burwitz, V., Schartel, N., & Hasinger, G. 2003, AN, 324, 27
Kormendy, J., & Ho, L. C. 2013, ARA&A, 51, 511
Koss, M., Mushotzky, R., Treister, E., et al. 2011, ApJL, 735, L42
Kulkarni, G., & Loeb, A. 2012, MNRAS, 422, 1306
Liao, W.-T., Chen, Y.-C., Liu, X., et al. 2021, MNRAS, 500, 4025
Liu, H.-Y., Liu, W.-J., Dong, X.-B., et al. 2019, ApJS, 243, 21

Liu, T., Gezari, S., Ayers, M., et al. 2019, ApJ, 884, 36
Liu, T., Koss, M., Blecha, L., et al. 2020, ApJ, 896, 122
Liu, X., Civano, F., Shen, Y., et al. 2013, ApJ, 762, 110
Liu, X., Greene, J. E., Shen, Y., & Strauss, M. A. 2010, ApJL, 715, L30
Liu, X., Guo, H., Shen, Y., Greene, J. E., & Strauss, M. A. 2018, ApJ, 862, 29
Liu, X., Shen, Y., & Strauss, M. A. 2011, ApJL, 736, L7
Lomb, N. R. 1976, Ap&SS, 39, 447
Lyu, J., Rieke, G. H., & Smith, P. S. 2019, ApJ, 886, 33
Ma, X.-C., & Wang, T.-G. 2013, MNRAS, 430, 3445
MacLeod, C. L., Ivezić, Ž, Kochanek, C. S., et al. 2010, ApJ, 721, 1014
Mainzer, A. K., Masiero, J. R., Abell, P. A., et al. 2023, PSJ, 4, 224
Mainzer, A., Bauer, J., Cutri, R. M., et al. 2014, ApJ, 792, 30
Masci, F. J., Laher, R. R., Rusholme, B., et al. 2019, PASP, 131, 018003
Merritt, D. 2013, Dynamics and Evolution of Galactic Nuclei (Princeton, NJ: Princeton Univ. Press)
O'Neill, S., Kiehlmann, S., Readhead, A. C. S., et al. 2022, ApJL, 926, L35
Planck Collaboration, et al. 2020, A&A, 641, A6
Rau, A., Kulkarni, S. R., Law, N. M., et al. 2009, PASP, 121, 1334
Sandrinelli, A., Covino, S., Treves, A., et al. 2018, A&A, 615, A118
Scargle, J. D. 1982, ApJ, 263, 835
Serafinelli, R., Covino, S., Treves, A., et al. 2020, ApJ, 902, 10
Shen, Y. 2009, ApJ, 704, 89
Shen, Y. 2013, BASI, 41, 61
Spergel, D., Gehrels, N., Baltay, C., et al. 2015, arXiv:1503.03757
VanderPlas, J. T. 2018, ApJS, 236, 16
Vaughan, S., Uttley, P., Markowitz, A. G., et al. 2016, MNRAS, 461, 3145
Wright, E. L., Eisenhardt, P. R. M., Mainzer, A. K., et al. 2010, AJ, 140, 1868
Wu, Q., & Shen, Y. 2022, ApJS, 263, 42
Zechmeister, M., & Kürster, M. 2009, A&A, 496, 577
Zheng, Z.-Y., Butler, N. R., Shen, Y., et al. 2016, ApJ, 827, 56
Zhou, H., Wang, T., Zhang, X., Dong, X., & Li, C. 2004, ApJL, 604, L33
Zu, Y., Kochanek, C. S., Kozłowski, S., & Udalski, A. 2013, ApJ, 765, 106